

# **Phase-change materials for volatile threshold resistive switching and neuronal device applications**

Huandong Chen<sup>1,4</sup>, Jayakanth Ravichandran<sup>1,2,3\*</sup>

<sup>1</sup>Mork Family Department of Chemical Engineering and Materials Science, University of Southern California, Los Angeles CA, USA

<sup>2</sup>Ming Hsieh Department of Electrical and Computer Engineering, University of Southern California, Los Angeles CA, USA

<sup>3</sup>Core Center for Excellence in Nano Imaging, University of Southern California, Los Angeles CA, USA

<sup>4</sup>Present Address: Condensed Matter Physics and Materials Science Department, Brookhaven National Laboratory, Upton NY, USA

\*Email: [j.ravichandran@usc.edu](mailto:j.ravichandran@usc.edu)

## **Abstract**

Volatile threshold resistive switching and neuronal oscillations in phase-change materials, specifically those undergoing metal-to-insulator and charge density wave transitions, offer unique attributes such as fast and low-field volatile switching, tunability, and non-linear behaviors. These characteristics are particularly promising for emulating neuronal behavior and thus hold great potential for realizing energy-efficient neuromorphic computing. In this review, we summarize recent advances in the development of neuronal oscillator devices based on three archetypal electronic phase-change materials: the correlated oxide  $\text{VO}_2$ , the charge density wave transition metal dichalcogenide  $1T\text{-TaS}_2$ , and the emerging phase-change chalcogenide perovskite  $\text{BaTiS}_3$ . We discuss progress from the perspective of materials development, including structural phase transitions, synthesis methods, electrical properties, and device implementation. Finally, we emphasize the major challenges that must be addressed for practical applications of these phase-change materials and provide our outlook on the future research directions in this rapidly evolving field.

**Keywords:** phase-change materials; metal-to-insulator transition; Mott insulator; charge density wave; volatile switching; neuronal functionalities

## 1. Introduction

Due to the recent slowdown in Moore's law and the increasing computational demands of artificial intelligence applications,<sup>1-3</sup> the development of novel "post-complementary metal-oxide-semiconductor (CMOS)" hardware that is both energy-efficient and capable of handling complex tasks has become highly sought after.<sup>4,5</sup> Neuromorphic computing, a paradigm that interconnects networks of artificial synapses and neuronal devices, can physically emulate the structure and function of the human brain, offering remarkably low power consumption and intrinsic learning capabilities.<sup>6-10</sup> Figure 1a illustrates a biological neuron specialized for processing and transmitting cellular signals, whereas Figure 1b shows a typical tonic firing pattern of single neuron exhibiting rhythmic spiking activity.<sup>11</sup> Early attempts to mimic the neuronal and synaptic behavior of brain used non-von Neumann architectures based on conventional CMOS circuits and metal-oxide memristors, enabling the demonstration of millions of programmable spiking neurons constructed from billions of transistors.<sup>12,13</sup> However, such systems remain far away from true brain-like operation, primarily due to its low energy efficiency and limited system complexity.

Alternatively, researchers have pursued novel materials and device architectures that leverage intriguing physical phenomena to emulate synaptic and neuronal functionalities. A range of non-volatile devices, including memristors,<sup>14-16</sup> phase change memory,<sup>17,18</sup> ferroelectric memory,<sup>19-21</sup> and magnetic tunnel junctions,<sup>22-24</sup> have been developed as synaptic components in integrated neuromorphic systems. Meanwhile, materials exhibiting volatile threshold switching mechanisms, such as metallic filament type,<sup>25,26</sup> thermal feedback,<sup>27,28</sup> ferroelectric,<sup>29,30</sup> and electronic phase transitions,<sup>31-34</sup> are often employed as neuronal devices. Among these, phase change materials, with well-defined structural and electronic phase transitions (metal-to-insulator

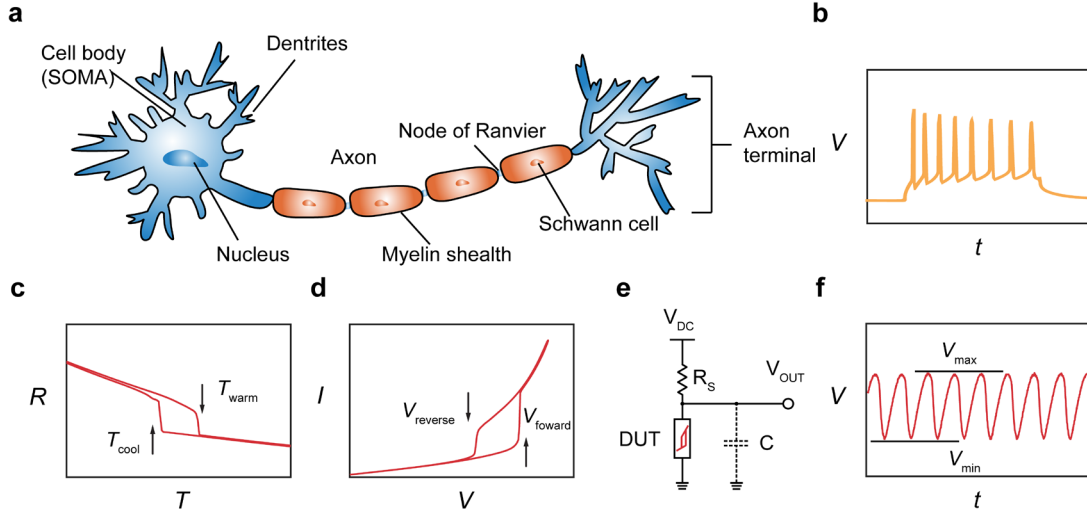


**Figure 1** (a) Schematic illustration of the structure of a biological neuron. (b) Representative tonic firing pattern of a single neuron showing spiking activity. (c) Typical temperature-dependence of electrical resistance of a phase-change material showing electronic phase transitions. (d) Typical  $I$ - $V$  characteristics of volatile threshold resistive switching in a phase change material driven by DC voltages. (e) and (f) Representative circuit diagram for introducing voltage oscillations in a two-terminal phase-change volatile resistive switching device and the corresponding oscillation waveform. (c) to (f) Figures adapted from Ref. [34] Copyright 2023, John Wiley & Sons.

type), are especially promising for mimicking the oscillatory and dynamic features of biological neurons, owing to their high complexity, as illustrated in Figure 1c to 1f.

Extensive research interests on metal-insulator transitions and the associated voltage-triggered resistive switching originated from Morin's pioneering work on phase transitions in binary transition metal oxides in late 1950s.<sup>35</sup> He observed that the resistance of certain binary transition metal oxides, such as vanadium oxides ( $\text{VO}_2$ ,  $\text{V}_2\text{O}_3$ , and  $\text{VO}$ ) and titanium sesquioxide ( $\text{Ti}_2\text{O}_3$ ), increases by several orders of magnitude upon crossing a characteristic temperature ( $T_C$ ).<sup>35</sup> As sister compounds of vanadium oxides, niobium oxides (e.g.,  $\text{NbO}_2$ ) also undergo metal-to-insulator transitions in similar manners, albeit at notably higher transition temperatures.<sup>36,37</sup> Later, rare-earth nickelate perovskites,  $\text{LnNiO}_3$  (where  $\text{Ln} = \text{Pr}, \text{Nd}, \text{Sm}$ ), were reported to exhibit similar metal-to-insulator transitions, in both bulk form and strained thin films.<sup>38,39</sup> These metal-

to-insulator transitions in oxides are predominantly attributed to Mott transition, which arises from strong electron-electron correlations.<sup>40-42</sup>

It is also noteworthy that, according to Peierls' toy model, the metal-to-insulator transition is among the key characteristics of a charge-density-wave (CDW) transition, which arises from strong electron-phonon interactions; however, it does not manifest in every real CDW material.<sup>43</sup> For instance, the  $1T$  phase of the transition metal dichalcogenide TaS<sub>2</sub> exhibits pronounced resistivity jumps across CDW transitions, as first observed by Thompson *et.al.* in the early 1970s.<sup>44</sup> With advances in 2D device fabrication and testing, interest in utilizing TaS<sub>2</sub> for neuronal applications has grown markedly since the mid-2010s.<sup>45-47</sup> More recently, several emerging chalcogenide crystals, including BaTiS<sub>3</sub> and EuTe<sub>4</sub>, have been shown to host both CDW orders and metal-to-insulator transitions,<sup>34,48-50</sup> rendering them promising candidates to demonstrate resistive switching for emulating synaptic or neuronal functionalities. Note that due to the large hysteresis window in EuTe<sub>4</sub>, the resistive switching is non-volatile and tends to demonstrate memory effects.<sup>50</sup>

Several comprehensive, material-oriented reviews on phase change materials and their applications for neuromorphic computing have been available in the literature.<sup>51-53</sup> In this work, we focus explicitly on connecting the material properties of correlated oxides and emerging CDW materials that exhibit volatile resistive switching with neuronal device characteristics. We review three archetypal phase-change materials – namely the correlated binary oxide VO<sub>2</sub> and the CDW chalcogenides  $1T$ -TaS<sub>2</sub> and BaTiS<sub>3</sub> – and assess their potential for neuronal device applications from the perspective of materials development. Their intrinsic structural and electrical properties, device characteristics, as well as aspects of material synthesis and device fabrication are discussed.

## **2. Coincident structural and electronic phase transitions**

Electronic phase transitions often coincide with structural phase transitions. Although the underlying mechanisms driving these electronic phase transitions and the role of the structural transformations remain actively debated in many materials such as VO<sub>2</sub>, the concurrent occurrence of both phenomena is well documented.<sup>54,55</sup> Because these well-defined structural phase transitions are directly tied to the desired electrical characteristics in phase-change materials, elucidating the structural transitions is the crucial for understanding the limitations of device performance in resistive switching and voltage oscillations. In the correlated oxide VO<sub>2</sub>, a monoclinic-to-tetragonal structural transition occurs alongside a pronounced change in resistivity across the metal-to-insulator transition.<sup>54</sup> Meanwhile, in low-dimensional CDW chalcogenides such as 1T-TaS<sub>2</sub> and BaTiS<sub>3</sub>, the underlying periodic lattice distortions such as star-of-David structural transition (1T-TaS<sub>2</sub>)<sup>56</sup> and in-plane unit cell doubling (BaTiS<sub>3</sub>)<sup>48</sup> (Figure 2) coincide with the abrupt changes in the electrical properties.

## 2.1 Metal-to-insulator transitions: the case of VO<sub>2</sub>

The metal-to-insulator transition (MIT) in VO<sub>2</sub>, a strongly correlated oxide, was first reported by Morin in 1959, who observed changes of several orders of magnitude in electrical conductivity that couple with a structural transition from monoclinic to tetragonal.<sup>35</sup> As illustrated in Figure 2a, VO<sub>2</sub> adopts a monoclinic crystal structure at room temperature ( $a = 5.75 \text{ \AA}$ ,  $b = 4.52 \text{ \AA}$ ,  $c = 5.38 \text{ \AA}$ ,  $\alpha = \gamma = 90^\circ$ ,  $\beta = 122.6^\circ$ ) with a space group of  $P2_1/c$ . Above the transition temperature ( $T_c = 340 \text{ K}$ , or  $67^\circ \text{ C}$ ), the structure becomes tetragonal ( $a = b = 4.55 \text{ \AA}$ ,  $c = 2.85 \text{ \AA}$ ,  $\alpha = \beta = \gamma = 90^\circ$ ) with a space group of  $P4_2/mnm$ , analogous to rutile TiO<sub>2</sub>.

In 1971, Goodenough suggested that an antiferroelectric distortion and the formation of V-V homopolar bonds below  $T_c$  are responsible for the MIT in VO<sub>2</sub>.<sup>54</sup> Following his idea, electron-

phonon coupling, which is often referred to as the “Peierls origin”, has been widely used to explain the transition, wherein a lattice distortion modulates the periodic potential and alters the band structure.<sup>57,58</sup> Several experimental observations such as optical phonon softening at the  $R$  point of the Brillouin zone also supports this scheme.<sup>55</sup> Nevertheless, the pure Peierls-based picture cannot fully account for features such as the relatively large bandgap (0.6 eV) and the appearance of an intermediate monoclinic phase without considering electron-electron interactions.

In 1975, Zylbersztein and Mott argued that the insulating phase of VO<sub>2</sub> cannot be correctly described without taking into account the Hubbard correlation energy ( $U$ ), whereas the metallic phase properties are primarily governed by the band structure.<sup>59</sup> In the metallic phase, two  $d$ -bands overlap and screen out the electron interactions. The crystalline distortion lifts the band degeneracy such that the correlation energy becomes comparable to the bandwidth and hence, the MIT is triggered. The Mott’s criterion for the electronic transition is given as  $(n_c)^{1/3} \alpha_H \approx 0.25$ , where  $n_c$  denotes the critical carrier density and  $\alpha_H$  is the Bohr radius. In 2000, Stefanovich *et al.* found that the insulator-metal transition in VO<sub>2</sub> can be induced by injecting excessing carriers without heating up the lattice to  $T_c$ , which they construed as strong evidence for the electronic Mott-Hubbard scenario.<sup>60</sup> Moreover, in 2014, Morrison *et al.* reported a photoinduced metal-like monoclinic phase of VO<sub>2</sub>, observing that the latent heat of MIT is primarily associated with the structural changes, whereas the photoexcitation was insufficient to alter the underlying lattice distortion.<sup>61</sup> These findings suggest that both Peierls distortion and Mott correlation contribute to the MIT in VO<sub>2</sub>, and that they are closely connected through orbital occupancy. A theoretical study by Biermann *et al.* further postulates a correlation-assisted Peierls transition, wherein the electron-electron interactions facilitate the gap opening.<sup>62</sup> Nevertheless, the mechanisms or driving force of VO<sub>2</sub>’s phase transition remains the subject of ongoing research.

## 2.2 Charge density wave transitions

Charge density waves (CDW) have been reported in various layered transition metal dichalcogenides (TMDCs) such as  $1T$ -TaS<sub>2</sub>,  $2H$ -TaSe<sub>2</sub>, and  $1T$ -TiSe<sub>2</sub>, in addition to classic quasi-1D metals.<sup>63</sup> The two-dimensional compound TaS<sub>2</sub> belongs to the family of TMDCs and crystallizes in different layered structures, including the  $1T$  and  $2H$  polytypes.<sup>44,64</sup> In  $1T$ -TaS<sub>2</sub>, tantalum (Ta) atoms, octahedrally coordinated by surrounding sulfur atoms, are hexagonally arranged in plane (Figure 2b). In 1975, Scruby *et al.* carried out temperature-dependent electron and X-ray diffraction studies<sup>56,65</sup> to reveal three metastable phases in  $1T$ -TaS<sub>2</sub>. The material exhibits a metallic phase at high temperatures ( $a = b = 3.36 \text{ \AA}$ ,  $c = 5.90 \text{ \AA}$ ,  $\alpha = \beta = 90^\circ$ ,  $\gamma = 120^\circ$ ) with the  $P\bar{3}m1$  space group, and it switches to an incommensurate CDW (ICCDW) phase below 550 K. The diffraction pattern of the ICCDW phase is dominated by diffuse spots with an incommensurate wave vector  $q_{IC} = 0.283a^* + c^*/3$ . Upon further cooling to approximately 350 K, the wave vector rotates by about  $12^\circ$  toward  $q_{NC} = 0.245a^* + 0.068b^* + c^*/3$ , giving rise to a nearly commensurate CDW (NCCDW) phase. Finally, below 180 K, a commensurate CDW (CCDW) phase with a  $\sqrt{13}a \times \sqrt{13}b \times 13c$  supercell dominates, which corresponds to a commensurate wave vector of  $q_C = (3a^* + b^*)/13 = 0.2308a^* + 0.0769b^*$ .

In the CCDW phase, the star-of-David clusters form as twelve surrounding Ta atoms displace inward towards a central thirteenth Ta atom within each layer. In 1979, Fazekas and Tosatti proposed that out of the thirteen  $5d^1$  electrons, twelve become paired in ‘star-bonding’ orbitals, leaving the thirteenth electron localized near the cluster center.<sup>66</sup> As a result, only these



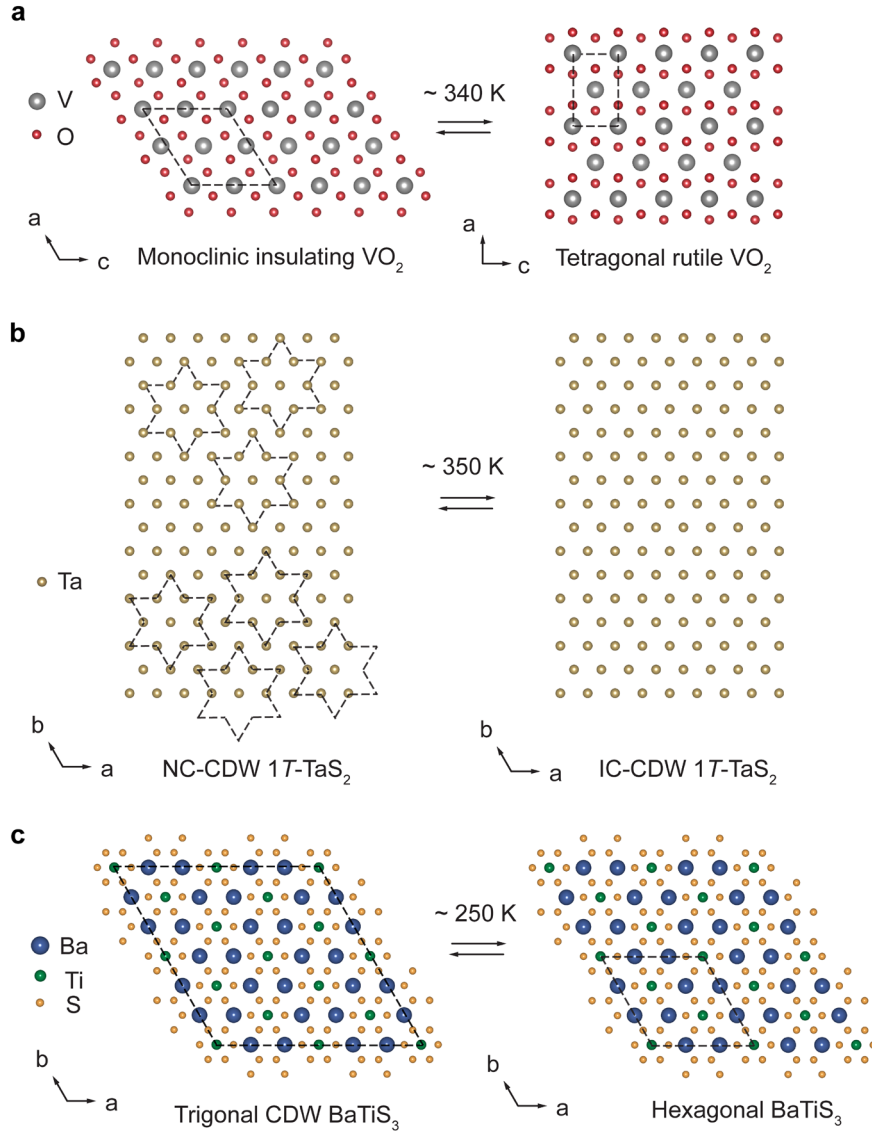


**Figure 2 Phase transitions.** Schematic illustration of structural phase transitions in (a) VO<sub>2</sub>, from tetragonal rutile phase to monoclinic phase at  $\sim 340$  K, (b) 1T-TaS<sub>2</sub>, from IC-CDW to NC-CDW phase at  $\sim 350$  K, and (c) BaTiS<sub>3</sub>, from hexagonal to trigonal phase at  $\sim 250$  K.

central electrons contribute to electrical conduction and magnetism. Therefore, a Mott-type localization may occur within the sub-band of these central electrons due to their large separations, which explains the drop in conductivity below 200 K. This electron localization scenario is further supported by Hall measurements performed by Inada *et al.* in 1979,<sup>67,68</sup> which demonstrated that the charge carrier density in the CCDW state is an order of magnitude lower than what would be

expected from CDW-induced band gaps alone. As illustrated in Figure 3b, the NCCDW phase also contains star-of-David clusters, albeit arranged in a less uniform pattern. Notably, the structural transition between the NCCDW and ICCDW phases is highly relevant for electrically induced threshold switching and voltage oscillations in 1T-TaS<sub>2</sub> devices operating at room temperature.

Unlike conventional metallic CDW materials, the quasi-1D chalcogenide BaTiS<sub>3</sub> is a small bandgap  $d^0$  semiconductor with a bandgap of approximately 0.3 eV.<sup>69</sup> At room temperature, BaTiS<sub>3</sub> adopts a hexagonal crystal structure ( $a = b = 11.7 \text{ \AA}$ ,  $c = 5.83 \text{ \AA}$ ,  $\alpha = \beta = 90^\circ$ ,  $\gamma = 120^\circ$ ) with a space group of  $P6_3cm$ .<sup>48</sup> In 2018, Niu *et al.* reported a giant optical anisotropy with a record-high birefringence in single crystals of BaTiS<sub>3</sub>, sparking significant research interest in this material.<sup>69</sup> Because of its nominally empty conduction band, no phase transition was initially expected for BaTiS<sub>3</sub>, even though its  $d^1$  counterpart, BaVS<sub>3</sub>, is considered an archetypical CDW system with a magnetic transition.<sup>70,71</sup> In 2023, Chen *et al.* experimentally demonstrated the presence of CDW order and a series of phase transitions in BaTiS<sub>3</sub> using electrical transport measurements and temperature-dependent synchrotron X-ray diffraction.<sup>48</sup> Upon cooling from room temperature to approximately 240 K, a structural transition takes place with titanium atoms displacing in  $a$ - $b$  plane, which leads to a lattice unit cell doubling ( $a = b = 23.3 \text{ \AA}$ ,  $c = 5.84 \text{ \AA}$ ,  $\alpha = \beta = 90^\circ$ ,  $\gamma = 120^\circ$ ) and hence a new CDW phase with a space group of  $P3c1$ , as illustrated in Figure 2c. Key evidence for the CDW includes the emergence of weak superlattice reflections in the diffraction pattern and the corresponding resistivity anomalies observed from transport measurements.<sup>48</sup> Further cooling to 130 K causes these superlattice peaks to disappear while a new set of reflections associated with a smaller  $\frac{2}{\sqrt{3}} \times \frac{2}{\sqrt{3}}$  unit cell ( $a = b = 13.4 \text{ \AA}$ ,  $c = 5.82 \text{ \AA}$ ,  $\alpha = \beta = 90^\circ$ ,  $\gamma = 120^\circ$ ) emerges. This observation indicates a suppression of the CDW phase *via* the

structural transition from  $P3c1$  to  $P2_1$ . Consistently, transport measurements reveal two hysteretic transitions in the 150 K – 190 K and 240 – 260 K ranges, respectively.<sup>48</sup>

The mechanisms driving these phase transitions in a gapped semiconductor such as  $\text{BaTiS}_3$  can be complicated. Because its Fermi level lies within the bandgap, there is no conventional concept of Fermi surface; thus, the nesting mechanism associated with quasi-1D CDW metals does not apply.<sup>48</sup> Hall measurements reveal a low carrier concentration of  $\sim 1.1 \times 10^{18} \text{ cm}^{-3}$  at room temperature, which further drops to less than  $10^{15} \text{ cm}^{-3}$  at 100 K.<sup>48</sup> In such a non-degenerate system with dilute concentration of electrons, the role of electron-electron interaction in  $\text{BaTiS}_3$  can be nontrivial, unlike most metallic or semi-metallic CDW compounds. Therefore, Chen *et.al.* suggested that both electron-lattice coupling and non-negligible electron-electron interactions contribute to the observed CDW order and phase transitions in semiconducting  $\text{BaTiS}_3$ .<sup>48</sup>

### **3. Materials synthesis**

This section provides an overview of the synthesis routes employed for the three phase-change material systems covered in this review ( $\text{VO}_2$ ,  $1T\text{-TaS}_2$ , and  $\text{BaTiS}_3$ ). Owing to their distinct chemistries, physical properties, and different levels of research focus since their initial discoveries, the methods used to synthesize these materials vary significantly. In general, single-crystal forms of materials are preferred in early days of research for studying their intrinsic physical properties and the demonstration of prototype devices. By contrast, large-area, high-quality thin film growth is usually crucial for realizing practical electronic device applications.

#### **3.1 Bulk single crystal synthesis**

In 1959, Morin conducted the first electrical transport study of various oxides showing MIT, such as  $\text{Ti}_2\text{O}_3$ ,  $\text{VO}$ ,  $\text{V}_2\text{O}_3$ , and  $\text{VO}_2$ .<sup>35</sup> In his work, single crystals of vanadium oxides were synthesized *via* a hydrothermal process. The details of the crystal growth using this method can be found in a subsequent book chapter by Laudise and Nielsen.<sup>72</sup> At that time, however, the single-crystal samples were on the order of 0.1 mm in size, which were too small for standard four-point measurements. Consequently, the observed electrical conductivity change across the MIT in  $\text{VO}_2$  was limited to merely two orders of magnitude,<sup>35</sup> likely due to significant contact resistances in two-probe geometry. Thereafter, a variety of advanced synthesis methods have been developed to produce high-quality and large-sized  $\text{VO}_2$  single crystals. For instance, in 1969, Ladd and Paul employed a molten-flux technique to grow millimeter-scale  $\text{VO}_2$  single crystals using  $\text{V}_2\text{O}_5$  as flux.<sup>73</sup> These crystals showed a  $10^5$ -fold change in resistivity near 340 K, which is widely considered the benchmark performance for  $\text{VO}_2$ .<sup>73</sup> In 1971, Nagasawa adopted a chemical vapor transport (CVT) method<sup>74</sup> to obtain single crystals of vanadium oxides using  $\text{TeCl}_4$  as a transport agent,<sup>75</sup> and in 1972, Reyes *et al.* succeeded in synthesizing doped  $\text{VO}_2$  single crystals *via* an isothermal flux evaporation method.<sup>76</sup>

Single crystals of  $1T$ - $\text{TaS}_2$  are commonly obtained by the CVT technique, like many other layered TMDCs, as illustrated in Figure 3d. A comprehensive review of this method can be found in the book by Schäfer (1964).<sup>77</sup> By 1969, Wilson and many other researchers had succeeded in synthesizing TMDCs single crystals (including  $\text{TaS}_2$ ) with dimensions up to a centimeter.<sup>64</sup> Iodine ( $\text{I}_2$ ) serves as the most widely used transport agent, although bromine and chlorine are occasionally employed. Typically,  $\sim 1 \text{ mg/cm}^3$  of  $\text{I}_2$  is placed in a sealed quartz ampule to balance an efficient

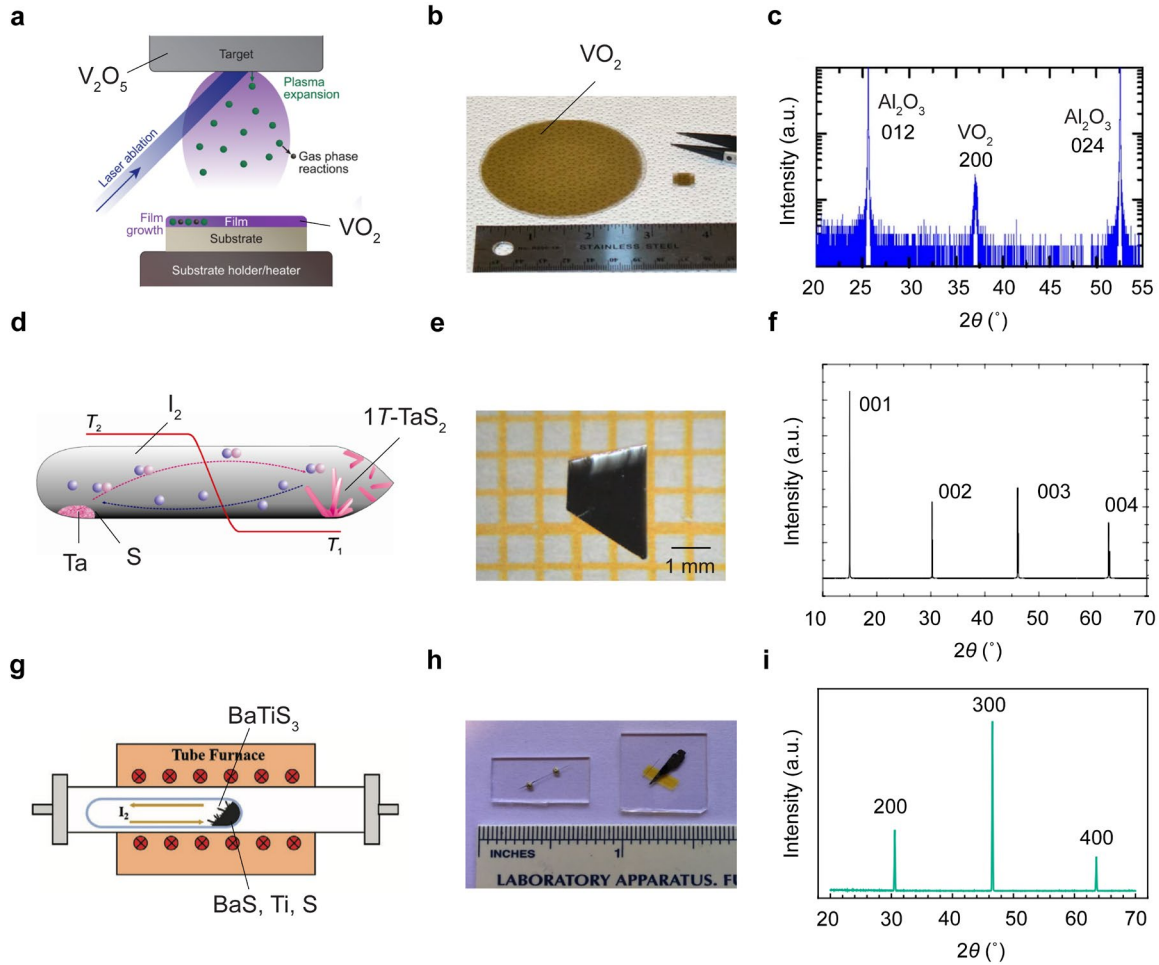


**Figure 3 Material synthesis.** (a) Schematic illustration of a PLD system for epitaxial thin film growth of VO<sub>2</sub> using a V<sub>2</sub>O<sub>5</sub> target. Figure adapted from Ref. [88] Copyright 2023, Royal Society of Chemistry. (b) Optical image of VO<sub>2</sub> thin films grown on a 3-inch sapphire substrate and a regular 5 mm substrate. (c) The corresponding XRD scan of the VO<sub>2</sub> thin film grown on sapphire. (b) and (c) Figures adapted from Ref. [94] Copyright 2015, Springer Nature. (d) Schematic illustration of 1T-TaS<sub>2</sub> single crystal growth using a CVT method. The schematic is adapted from Ref. [74] Copyright 2013, Intech Open. (e) Optical image of a large-sized 1T-TaS<sub>2</sub> single crystal. (f) The corresponding out-of-plane XRD scan of the 1T-TaS<sub>2</sub> crystal. (e) and (f) Figures adapted from Ref. [78] Copyright 2015, Springer Nature. (g) Schematic illustration of BaTiS<sub>3</sub> single crystal synthesis using a vapor transport method. Figure adapted with permission from Ref. [81] Copyright 2022, John Wiley & Sons. (h) Optical image of the representative as-grown BaTiS<sub>3</sub> crystals with needle-like and plate-like morphologies. (i) Out-of-plane XRD scan of a BaTiS<sub>3</sub> plate with *a*- and *c*-axes in plane. (h) and (i) Figures adapted with permission from Ref. [69] Copyright 2018, Springer Nature.

reaction rate with minimal unintentional iodine incorporation. Figure 3e displays an optical image of a representative bulk 1T-TaS<sub>2</sub> crystal (2 mm × 3 mm), and Figure 3f illustrates an XRD scan of

the same sample.<sup>78</sup> In 1971, Thompson *et al.* prepared single crystals of  $1T$ -TaS<sub>2</sub> by quenching sealed ampules from  $\sim 950^\circ\text{C}$ , following a CVT crystal growth recipe that used pre-reacted  $2H$ -TaS<sub>2</sub> powder as the starting materials and I<sub>2</sub> as the transport agent.<sup>44</sup> Notably, the  $1T$  polymorph of TaS<sub>2</sub> is thermodynamically stable at temperatures above  $777^\circ\text{C}$  ( $\sim 1050$  K) in its phase diagram, and therefore, growths with slow cooling will lead to  $2H$ -TaS<sub>2</sub>, which is metallic and becomes superconducting below 0.8 K.<sup>66</sup> With sufficiently large crystal sizes, Thompson *et al.* further performed transport measurements up to 400 K using a van der Pauw geometry, revealing the intrinsic electrical transport behavior of bulk  $1T$ -TaS<sub>2</sub> featuring two metal-to-insulator phase transitions<sup>44</sup>. Those two transitions were later assigned as the CCDW-to-NCCDW and NCCDW-to-ICCDW transitions, respectively. Due to the upper limit of the measurement temperature, the higher-temperature metallic phase was not captured in that study.<sup>44</sup>

In contrast to VO<sub>2</sub> and  $1T$ -TaS<sub>2</sub>, BaTiS<sub>3</sub> has received far less attention as a phase-change material, and its single-crystal form was not available prior to 2018, despite the synthesis and structural characterization of BaTiS<sub>3</sub> powders dating back to 1957.<sup>79</sup> In 1996, Imai *et al.* measured the specific heat of pressed BaTiS<sub>3</sub> powder from 1.4 K to 300 K, but they did not observe any anomaly indicative of phase transitions.<sup>80</sup> The absence of observable transitions remains puzzling; one plausible hypothesis is that powders of BaTiS<sub>3</sub> contain significantly more point and extended defects than single crystals, thereby suppressing the transitions. Further thermodynamic studies of large, high-quality BaTiS<sub>3</sub> single crystals are expected to clarify this issue.

In 2018, Niu *et al.* reported the first successful growth of BaTiS<sub>3</sub> single crystals using a vapor-phase growth approach with I<sub>2</sub> as the transport agent.<sup>69</sup> Unlike many conventional CVT processes where source materials are transported towards the other end of the ampule, clusters of needle-like BaTiS<sub>3</sub> crystals (typically  $< 50$   $\mu\text{m}$  in both width and thickness) were observed to

directly grow out of BaTiS<sub>3</sub> powder,<sup>69</sup> as subsequently confirmed by Yang *et al.* in 2022<sup>81</sup> (Figure 3g). Slightly different from Niu's synthesis recipe, Yang *et al.* employed a larger temperature gradient to achieve a rapid growth process.<sup>81</sup> Beyond these needle-like morphologies, Niu *et al.* also obtained thin platelets of BaTiS<sub>3</sub> with *a*- and *c*- axes in plane that are suitable for optical studies, as shown in Figure 3h. Figure 3i illustrates a representative out-of-plane X-ray diffraction scan of such a plate-like BaTiS<sub>3</sub> crystal. These samples facilitated the full characterization of BaTiS<sub>3</sub>'s giant optical anisotropies, with a record-high birefringence of up to 0.76 in the mid- to long-infrared range.<sup>69</sup> Subsequently, Zhao *et al.* synthesized thin flakes of 001-type BaTiS<sub>3</sub> flakes with *a*- and *b*-axes in plane through a similar CVT route, albeit with slightly modified conditions<sup>82</sup>.

Despite the high quality of CVT-grown BaTiS<sub>3</sub> crystals that do exhibit intrinsic phase transitions, their sizes remain limited by the excess number of nucleation sites (powder) during growth, making the vapor transport method less suitable for the production of larger crystals. Recently, Chen *et al.* developed a molten-flux approach using either potassium iodide (KI) or a mixture of barium chloride (BaCl<sub>2</sub>) and barium iodide (BaI<sub>2</sub>) to grow BaTiS<sub>3</sub> crystals.<sup>83</sup> The KI-based flux approach yielded crystals of dimensions up to a centimeter in length and 500 μm in both width and thickness, whereas the BaCl<sub>2</sub>-BaI<sub>2</sub> flux method produced plate-like, (001)-oriented BaTiS<sub>3</sub> crystals up to 200 μm thick. These flux-grown crystals exhibit substantially larger volumes than those obtained *via* vapor transport, while preserving the material's intrinsic optical and electronic properties.<sup>83</sup> Such advancements in flux-based crystal growth not only facilitate the development of BaTiS<sub>3</sub>-based devices for optical and optoelectronic applications, but also enable advanced material characterizations, including neutron diffraction and scattering, to elucidate the underlying electronic phase transition mechanisms in this material.<sup>83</sup>

### 3.2 Thin film growth

Research efforts on synthesizing VO<sub>2</sub> thin films have been predominantly centered on using reactive magnetron sputtering<sup>84,85</sup> and pulsed laser deposition (PLD),<sup>86-89</sup> although other methods including molecular beam epitaxy (MBE),<sup>90,91</sup> metal-organic chemical vapor deposition (MOCVD),<sup>92</sup> and sol-gel routes<sup>93,94</sup> have also been investigated. In 1967, Fuls *et al.* synthesized VO<sub>2</sub> thin films by reactive sputtering from a vanadium target in an argon atmosphere with a controlled oxygen partial pressure.<sup>84</sup> These films, grown at 400°C on sapphire substrates, exhibited a highly orientated monoclinic phase at room temperature.<sup>84</sup> The MIT in these sputtered films was characterized by a 10<sup>4</sup>-fold change in resistivity and a thermal hysteresis of 9 K across the transition.<sup>84</sup> Because the magnitude of resistivity change and the width of the thermal hysteresis are highly sensitive to stoichiometry and crystallinity, these parameters serve as key indicators of VO<sub>2</sub> film quality. beginning in the late 1980s, PLD emerged as a versatile technique for synthesizing high-quality oxide thin films (Figure 3a). Its compatibility with relatively high oxygen pressures makes it particularly suitable for depositing stoichiometric oxides. In 1994, Kim and Kwok demonstrated high-quality VO<sub>2</sub> thin films on (0001) and (100) sapphire substrates by PLD, using pressed V<sub>2</sub>O<sub>3</sub> powder as the target.<sup>86</sup> The films grown on (100) substrates showed up to 10<sup>5</sup>-fold change in resistivity and a narrow thermal hysteresis of 1 K, which are comparable to those of a VO<sub>2</sub> single crystal, although the transition temperature was reduced to ~ 330 K due to epitaxial strain effects.<sup>86</sup> More recently, Zhang *et al.* reported wafer-scale VO<sub>2</sub> growth on sapphire substrates (Figure 3b) with a large resistance jump of ~ 10<sup>4</sup> through a hybrid-MBE approach. Figure 3c shows a representative XRD scan of such a VO<sub>2</sub> film<sup>95</sup>.

Thus far, most existing thin 1T-TaS<sub>2</sub> devices have been fabricated by mechanically exfoliating bulk crystals. While this method yields high-quality flakes, it restricts both sample size



and fabrication throughput. As a result, establishing large-area, controllable, and high-quality thin-film synthesis of  $1T$ -TaS<sub>2</sub> is crucial for advancing both fundamental studies – especially at the thin limit – and practical device applications. In 2016, Fu *et al.* demonstrated a chemical vapor deposition (CVD) approach to grow  $1T$ -TaS<sub>2</sub> thin flakes of varying thickness on SiO<sub>2</sub>/Si substrates, using TaCl<sub>5</sub> and sulfur powder as precursors under an H<sub>2</sub>/Ar atmosphere at 1093 K.<sup>96</sup> More recently, in 2018, Lin *et al.* developed an MBE growth method for TaS<sub>2</sub> on graphene-terminated  $6H$ -SiC (0001) substrates.<sup>97</sup> At a growth temperature of  $\sim 700^\circ\text{C}$ , both  $1T$  and  $2H$  phases of TaS<sub>2</sub> were obtained, and the authors suggested that higher substrate temperatures favor the formation of the  $1T$  phase.<sup>97</sup>

Thin-film growth of BaTiS<sub>3</sub> has, to date, been realized exclusively *via* PLD approaches developed for complex chalcogenides.<sup>98-100</sup> In 2022, Surendran *et al.* demonstrated the quasi-epitaxial synthesis of BaTiS<sub>3</sub> on single-crystalline SrTiO<sub>3</sub> substrates at approximately  $700^\circ\text{C}$ , using an Ar/H<sub>2</sub>S (5%) background atmosphere.<sup>98</sup> X-ray diffraction revealed a pronounced out-of-plane texture in these films, although but no clear in-plane epitaxial relationship between thin film and the substrate was observed.<sup>98</sup> More recently, Surendran *et al.* developed a hybrid PLD strategy that employs an organosulfur precursor as the background sulfur source, substituting the chemically aggressive Ar/H<sub>2</sub>S environment.<sup>99</sup> BaTiS<sub>3</sub> films grown on SrTiO<sub>3</sub> using this hybrid PLD method exhibited substantially improved surface and interface smoothness, while retaining crystallinity comparable to that achieved by conventional PLD using Ar/H<sub>2</sub>S.<sup>99</sup> Despite these advances, one of the main hurdles in realizing high-quality epitaxial ternary chalcogenide thin films is the scarcity of lattice-matched and chemically compatible substrates. Consequently, achieving wafer-scale complex chalcogenides through advanced single-crystal synthesis techniques such as top-seeded

solution growth or Bridgeman method, represents a vital step towards realizing high-quality chalcogenide thin films and their heterostructures.

#### **4. Device fabrication**

This section provides an overview of the recent advancements in electrical contact and device fabrication processes for three phase-change materials – VO<sub>2</sub> (thin films), 1T-TaS<sub>2</sub> (mechanically cleaved thin flakes), and BaTiS<sub>3</sub> (micro-scale bulk crystals). Owing to the different susceptibilities of these materials' phase transitions to external factors such as oxidation and strain, researchers have developed and implemented various strategies to preserve intrinsic transport properties and achieve the desired device performance.

Fabrication processes for VO<sub>2</sub> tend to be the most straightforward among the three materials, largely owing to the availability of high-quality thin films whose monoclinic-to-tetragonal phase transition is well-preserved.<sup>84,86</sup> Hence, conventional cleanroom micro-fabrication techniques, including photolithography, etching and metal deposition, can be readily applied. Device geometries of VO<sub>2</sub> such as multi-terminal Hall bars or linear bars are often patterned through dry etching approaches such as reactive ion etching (RIE) or ion milling for proper transport measurements.<sup>101-103</sup> In contrast, simpler two-terminal geometries are generally sufficient for neuronal oscillator devices (Figure 4a and 4b), where a short channel length proves crucial to achieving low switching voltages and high oscillation frequencies.<sup>101,104</sup> When device dimensions must be reduced beyond the limits of standard photolithography, an out-of-plane VO<sub>2</sub> device geometry, where the channel dimension is equivalent to the film thickness (on the order of tens of nanometers), is often employed.<sup>105,106</sup> In such configurations, VO<sub>2</sub> films are typically deposited on high-temperature-compatible conductive substrates, including Pt, TiN, and SrRuO<sub>3</sub>,

before putting down top electrodes.<sup>87,105,106</sup> In 2015, Mian *et al.* reported a record-high oscillation frequency of 9 MHz from a VO<sub>2</sub>/TiN device,<sup>105</sup> as illustrated in Figure 4c. Additional optimization of metal-to-VO<sub>2</sub> contacts is expected to further improve the device performance.

1T-TaS<sub>2</sub> exhibits a layered structure bonded *via* weak van der Waals interactions, and hence, it can be mechanically exfoliated down to a few tens of nanometers or thinner for device fabrication. Notably, there has been a long history of research on exfoliation and transfer of layered TMDCs,<sup>64,107</sup> dating back well before the discovery of single-layer graphene in 2004.<sup>108,109</sup> For instance, in 1962, Frindt and Yoffe produced ultra-thin molybdenum disulfide (MoS<sub>2</sub>) flakes (< 10 nm) by mechanical cleavage for optical and electron diffraction studies.<sup>107</sup> By 1969, Wilson and Yoffe were able to prepare thin specimens (<100 nm) of various TMDCs by repeated cleaving on adhesive tapes.<sup>64</sup> More recently, atomically thin 1T-TaS<sub>2</sub> has re-attracted enormous research interest, revealing novel phenomena such as gate-tuned phase transition,<sup>78</sup> electrical oscillations,<sup>45,47</sup> and memristive switching.<sup>46,110</sup> These advances have been facilitated by the fast-evolving developments of exfoliation and transfer techniques for 2D materials, wherein thin flakes of 1T-TaS<sub>2</sub> with thickness down to monolayer can be isolated and integrated into devices.

However, limited by the lateral dimensions of exfoliated flakes, especially those at the thin limit, e-beam lithography is often required to pattern fine features at the micrometer scale or smaller, and to accommodate the specific alignment requirement for each flake. Additionally, *h*BN encapsulation is usually employed to preserve the intrinsic device performance of 1T-TaS<sub>2</sub> when working with ultrathin samples<sup>78,111</sup> (Figure 4e), due to the material's propensity to degradation in air (Figure 4d). While mechanical exfoliation is suitable for laboratory-scale research, it is not practical for large-area device fabrication. Consequently, further efforts need to be made on high-

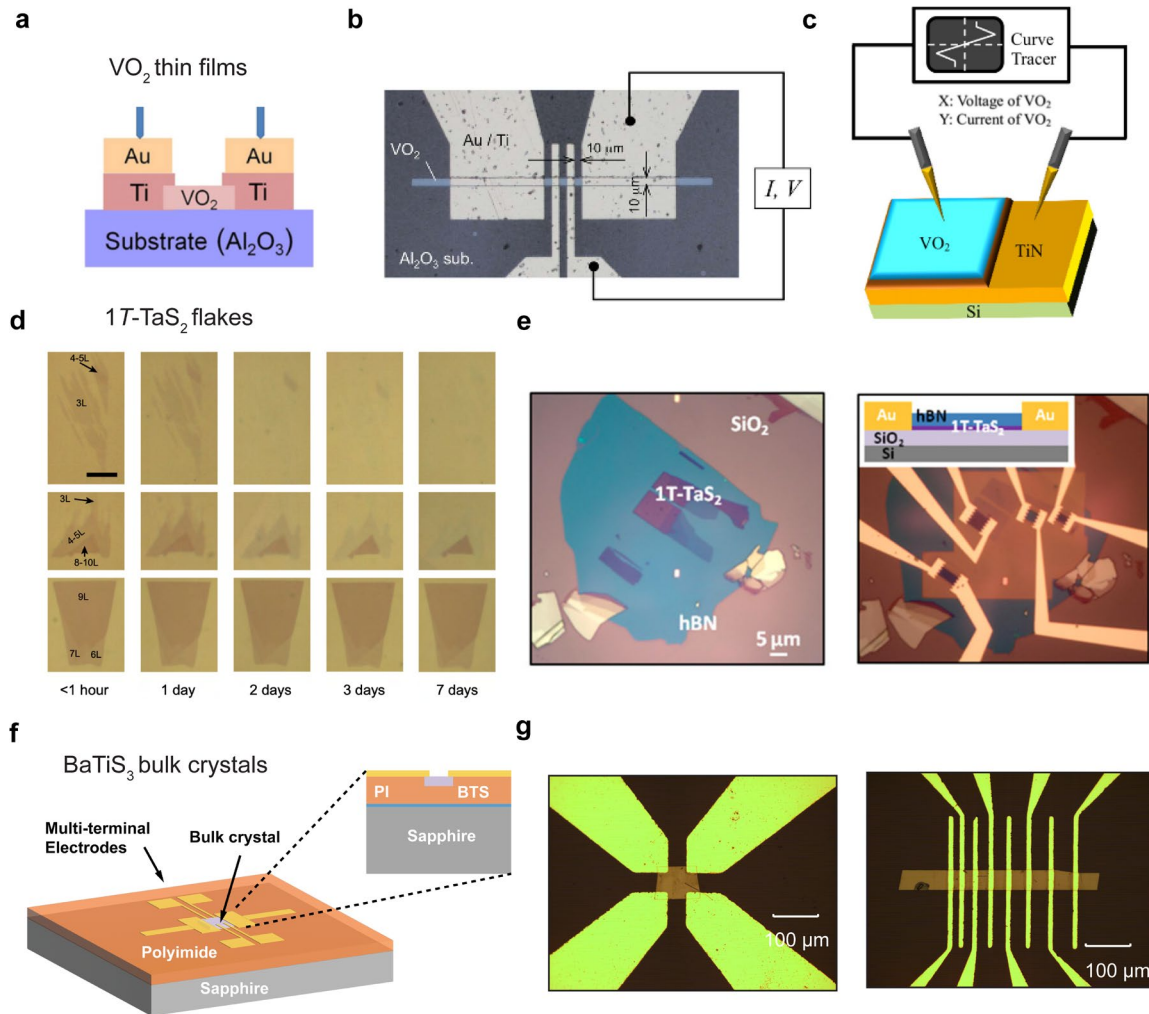


**Figure 4 Device Fabrication.** (a) Cross-sectional schematic of a two-terminal planar VO<sub>2</sub> thin film device. Figure adapted from Ref. [135] Copyright 2011, Elsevier. (b) Optical microscopic image of a four-probe VO<sub>2</sub> film device fabricated through dry etching. Figure adapted from Ref. [101] Copyright 2008, AIP Publishing. (c) Schematic illustration of an out-of-plane VO<sub>2</sub> film device using TiN as the bottom electrode. Figure adapted from Ref. [105] Copyright 2015, AIP Publishing. (d) Optical microscopic images of few-layer 1T-TaS<sub>2</sub> flakes showing the degradation progress in air. Figures adapted from Ref. [78] Copyright 2015, Springer Nature. (e) Optical microscopic images of device fabrication processes for mechanically exfoliated 1T-TaS<sub>2</sub> flakes on a SiO<sub>2</sub>/Si substrate, including hBN encapsulation (left) and metal deposition (right) steps. The inset to the right shows a cross-sectional schematic of the device. Figure adapted from Ref. [111] Copyright 2015, National Academy of Science. (f) Schematic illustration of a multi-terminal BaTiS<sub>3</sub> bulk device fabricated through polymeric planarization and regular photolithography processes. Figure adapted from Ref. [118] Copyright 2022, ACS Publications. (g) Optical microscopic images of BaTiS<sub>3</sub> bulk devices with a van der Waals (left) and a transmission line method (TLM, right) contact geometry. Figures adapted from Ref. [48] Copyright 2023, John Wiley & Sons.

quality thin-film synthesis of 1T-TaS<sub>2</sub>, where intrinsic electrical switching properties can be well-

preserved.<sup>96,97</sup>

For bulk crystals with lateral dimensions of several millimeters or larger, manual bonding is the predominant method for establishing electrical contacts, wherein thin metal wires, including gold, platinum, or indium, are directly attached to the crystal surfaces using conductive epoxy or self-melting methods.<sup>112,113</sup> In some cases, a thin, pre-sputtered or evaporated Au layer is deposited through a showing mask to reduce the contact resistances.<sup>114</sup> Early transport measurements on VO<sub>2</sub> and 1*T*-TaS<sub>2</sub> also relied on this manual bonding method.<sup>35,44</sup> For instance, Morin used two pressure contacts in 1959 for conductivity measurements of sub-0.1 mm VO<sub>2</sub> single crystals, the size of which were too small for standard four-point measurements.<sup>35</sup> Likewise, in 1971, Thompson *et al.* measured temperature-dependent resistivity of single-crystal 1*T*-TaS<sub>2</sub> using van der Pauw geometry, and five-contact measurements were used to determine the Hall coefficient.<sup>44</sup> Notably, typical 1*T*-TaS<sub>2</sub> sample size used for Hall measurements with 6-probe Hall bar geometry can reach lateral dimensions of approximately 10 × 1.5 mm<sup>2</sup> laterally, as reported by Uchida *et al.* in 1978.<sup>115</sup>

For BaTiS<sub>3</sub>, like many other small, non-exfoliable crystals, establishing high-quality multiterminal electrodes on them has proven challenging due to their limited size. Although Niu *et al.* has demonstrated the synthesis of large, thin BaTiS<sub>3</sub> platelets with lateral dimensions of several millimeters *via* a vapor transport method in his original optical anisotropy study in 2018,<sup>69</sup> the yield of such large samples suitable for manual bonding remains low, due to the large number of nucleation sites during growth. Indeed, most BaTiS<sub>3</sub> crystals grown by CVT methods exhibit a needle-like shape that is typically tens of microns in thickness and width, and up to several millimeters along the chain axis, as confirmed by several recent reports.<sup>69,81</sup> In 2022, Chen *et al.* addressed this challenge by adapting a polymeric planarization technique, initially developed for handling micro-scale GaAs-based devices,<sup>116,117</sup> to fabricate multiterminal electrical contacts on

small, bulk BaTiS<sub>3</sub> crystals for electrical transport studies.<sup>118,119</sup> As depicted in Figure 4f, the crystals are first embedded in a low-stress polymeric matrix (e.g., polyimide) to achieve a planar top surface, enabling direct application of standard lithography and microfabrication processes for forming electrodes with desired geometries.<sup>118</sup> The choice of a low-stress polymer minimizes extrinsic thermal strain effects at low temperatures, which preserves intrinsic transport characteristics of BaTiS<sub>3</sub> that are highly susceptible to strains.<sup>48,118</sup> These prototype BaTiS<sub>3</sub> single-crystal devices (Figure 4g) exhibited clear signatures of phase transitions and enabled proof-of-concept demonstrations of electrical resistive switching and voltage oscillations.<sup>34,48</sup> Further research and development on high-quality BaTiS<sub>3</sub> thin-film synthesis that features intrinsically robust or tunable phase transitions, will help streamline its device fabrication and pave the way toward practical electronic devices applications of this emerging phase-change material.

## 5. Transport properties

Temperature-dependent electrical transport measurements are among the most important characterizations for phase-change materials. Upon varying the temperature, anomalies in electrical resistivity such as metal-to-insulator transitions can emerge near specific transition temperatures, typically reflecting an underlying structural transition and corresponding modification in the electronic structure. In addition to the classic MIT observed in the correlated oxide VO<sub>2</sub>,<sup>35</sup> both the CDW systems 1T-TaS<sub>2</sub> and BaTiS<sub>3</sub> display pronounced resistivity changes across the transitions.<sup>44,48</sup> It is important to note, however, that the MIT is not a universal feature in all real CDW materials, despite the prediction of Peierls' theory for ideal one-dimensional metals.<sup>120,121</sup> Detailed temperature-dependent Hall measurements, which probe the evolution of

carrier concentration and mobility, further provide important insights into the mechanisms governing these phase transitions.

Figure 5a illustrates a typical temperature-dependent resistivity (or conductivity) measurement of a VO<sub>2</sub> single crystal, which exhibits a resistivity of approximately 10 Ω·cm at room temperature and drops to below 10<sup>-4</sup> Ω·cm at high temperatures, resulting in a change up to five orders of magnitude across the MIT.<sup>122</sup> In 1973, Rosevear and Paul investigated transport properties of both semiconducting and metallic phases in VO<sub>2</sub> single crystals using an oscillating AC magnetic field,<sup>123</sup> as shown in Figure 5b. At the insulator-to-metal transition, the carrier concentration extracted from the Hall measurements increased by roughly a factor of  $5 \times 10^4$ , whereas the Hall mobility changed from about 0.5 cm<sup>2</sup>/(V·s) to 0.35 cm<sup>2</sup>/V·s.<sup>123</sup> It is important to note that the magnitude of resistivity change and the width of the hysteresis loop depend strongly on the material's quality. For instance, a typical VO<sub>2</sub> thin film grown by RF sputtering exhibits a three-order-of-magnitude resistivity changes and a 10 K hysteresis.<sup>124</sup> In contrast, high-quality VO<sub>2</sub> thin films synthesized *via* pulsed laser deposition can attain a resistivity change of up to five orders of magnitude with a 1 K hysteresis,<sup>86</sup> comparable to that observed in bulk single crystals.<sup>73,125</sup>

1T-TaS<sub>2</sub> exhibits two pronounced discontinuities in resistivity below 400 K, as illustrated in Figure 5c. Near 350 K, the NCCDW-to-ICCDW transition occurs with minimal thermal hysteresis. In contrast, the low-temperature transition at ~200 K between the CCDW and NCCDW phases exhibits a roughly 20-fold increase in resistivity and a large hysteresis spanning tens of kelvins.<sup>44</sup> The exact hysteresis width varies among samples, which is presumably associated with impurities, structural defects or other forms of disorder. In fact, the earliest electrical transport study on 1T-TaS<sub>2</sub> by Thompson *et al.* in 1971 reported hysteresis width as large as 100 K for the

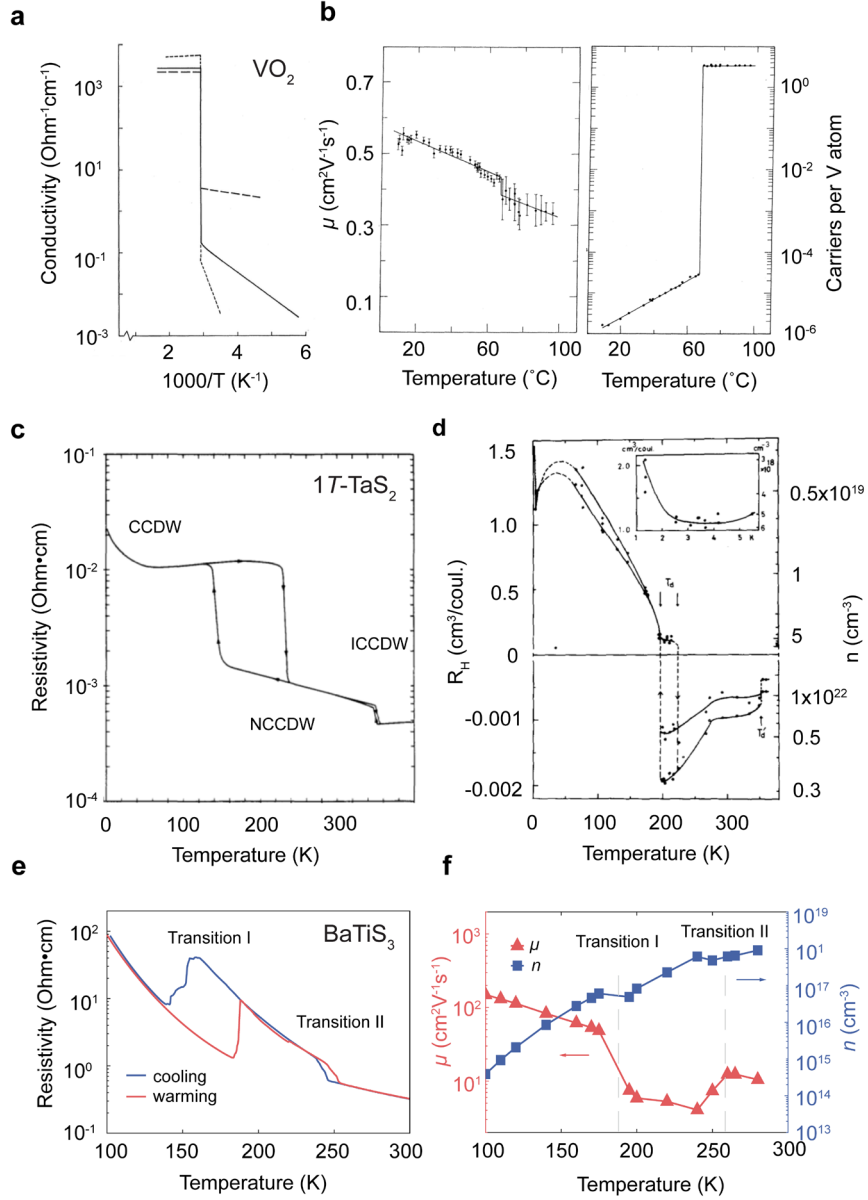


**Figure 5 Transport properties.** (a) Representative temperature dependence of the electrical conductivity of a VO<sub>2</sub> single crystal. Figure adapted from Ref. [122] Copyright 1969, American Physical Society. (b) Temperature evolution of Hall mobility (left) and carrier concentration (right) across the MIT phase transition in VO<sub>2</sub>. Figures adapted from Ref. [123] Copyright 1973, American Physical Society. (c) Representative temperature dependent resistivity of a 1T-TaS<sub>2</sub> crystal. Figure adapted from Ref. [44] Copyright 1971, Elsevier. (d) The corresponding temperature dependence of Hall coefficient and carrier concentration across the transitions. Figure adapted from Ref. [67] Copyright 1979, Elsevier. (e) Illustration of representative temperature dependent electrical resistivity of a BaTiS<sub>3</sub> crystal along the *c*-axis. (f) The corresponding temperature dependence of the mobility and carrier concentration. (e) and (f) Figures adapted from Ref. [48] Copyright 2023, John Wiley & Sons.

CCDW-to-NCCDW transition.<sup>44</sup> In 1980, Inada *et al.* found an even larger resistivity hysteresis of



150 K in  $1T$ -TaS<sub>1.2</sub>Se<sub>0.8</sub> single crystals, which was attributed to the increased disorder from selenium alloying.<sup>68</sup> Moreover, a sharp rise in resistivity is often observed at temperatures below  $\sim 50$  K. In 1977, Di Salvo and Graebner attributed this low-temperature increase in resistivity to an extrinsic Anderson localization effect by random impurities or defect potentials.<sup>126</sup>

Hall measurements of  $1T$ -TaS<sub>2</sub> provide further insights into its transport processes by revealing both the carrier type and concentrations, as demonstrated by Inada *et al.* in 1980 (Figure 5d).<sup>68</sup> The high-temperature metallic phase transforms into the ICCDW phase, where the Fermi surface is broken into fragments as a result of CDW formation. In this ICCDW phase, the residual Fermi surface fragments still give rise to a high carrier concentration of  $\sim 10^{22}$  cm<sup>-3</sup> and the majority carriers are electrons.<sup>68</sup> Upon crossing the NCCDW transition near 350 K, the carrier concentration drops by about 30%, and continues to decrease to  $\sim 3 \times 10^{21}$  cm<sup>-3</sup> down to  $\sim 200$  K. At the NCCDW-to-CCDW transition upon cooling, a discontinuous change in resistivity accompanies a sign reversal of the Hall coefficient ( $R_H$ ).<sup>68</sup> The system enters a semimetallic or semiconducting region with its majority carrier type switched to p-type at carrier concentrations of  $\sim 10^{19}$  cm<sup>-3</sup>.<sup>68</sup> A characteristic peak of  $R_H$  around 30-50 K is further postulated that, below that temperature range, the material becomes a semiconductor of the impurity type.<sup>68</sup>

Moreover, by simply reducing the thickness of  $1T$ -TaS<sub>2</sub>, researchers have significantly modulated its transport characteristics compared with bulk samples. In 2015, Yu *et al.* systematically investigated  $1T$ -TaS<sub>2</sub> thin flakes with varying thicknesses down to  $\sim 2$  nm, observing a pronounced broadening in the hysteresis width of the low-temperature NCCDW-to-CCDW transition as the thickness decreased from  $\sim 100$  nm to  $\sim 10$  nm, alongside a less abrupt overall resistivity change.<sup>78</sup> Below 10 nm, the CCDW-to-NCCDW transition is suppressed, whereas the higher-temperature NCCDW-to-CCDW transition at  $\sim 350$  K persists till  $\sim 4$  nm,

below which it also disappears.<sup>78</sup> However, debate continues regarding whether the apparent absence of CDW phase transitions in ultrathin, unprotected 1T-TaS<sub>2</sub> flakes arises from intrinsic dimensional effects or extrinsic factors such as oxidation. In late 2015, Tsen *et al.* demonstrated that ultrathin 1T-TaS<sub>2</sub> flakes, protected by hexagonal boron nitride (*h*BN), retained the NCCDW-to-CCDW transition at thickness down to 4 nm through both electron diffraction and transport measurements.<sup>111</sup> They even showed evidence of the NCCDW phase in the 2 nm sample using electron diffraction, although the transition to the CCDW was not observed at this thin limit.<sup>111</sup> These findings suggest that oxidization, rather than purely dimensional effects, may be responsible for the absence of charge order in ultrathin, unprotected 1T-TaS<sub>2</sub> flakes.<sup>111</sup>

In contrast, BaTiS<sub>3</sub> was not known to exhibit any phase transition until recently. In 2023, Chen *et al.* identified two distinct transitions in single-crystal BaTiS<sub>3</sub> from its non-monotonic, hysteretic transport behavior,<sup>48</sup> as shown in Figure 5e. Upon cooling, the system undergoes a transition from the ambient semiconducting phase to the CDW phase at ~ 240 K (“Transition II”) with a clear resistivity jump. On further cooling, the resistivity continues to rise till ~ 150 K, whereupon another transition (“Transition I”) drives the system into a high-conductivity state (or high-mobility state), marked by a sharp resistivity drop. The hysteresis spans over 40 K for Transition I and about 10 K for Transition II.<sup>48</sup> Structural characterizations revealed weak superlattice reflections indicative of a periodic lattice distortion emerging below Transition II, and these are subsequently suppressed at Transition I.<sup>48</sup> Below 100 K, the resistivity increases rapidly and becomes too large to measure reliably using standard AC transport techniques.

Hall measurements of BaTiS<sub>3</sub> single crystals further clarify its transport mechanisms.<sup>48</sup> With electron as majority carrier, BaTiS<sub>3</sub> has a room-temperature carrier concentration of ~  $1.1 \times 10^{18} \text{ cm}^{-3}$ , which is among the lowest reported for known CDW compounds, confirming its

nondegenerate nature.<sup>48</sup> As illustrated in Figure 5f, the carrier concentration decreases monotonically upon cooling, reaching  $\sim 10^{15} \text{ cm}^{-3}$  by 100 K, without any abrupt changes in magnitude or sign across either transition.<sup>48</sup> Instead, Hall mobility undergoes a significant drop and then a substantial rise at Transition II and I, respectively, suggesting that the modulation of BaTiS<sub>3</sub>'s resistance stems largely from variations in mobility.<sup>48</sup> This contrasts notably with VO<sub>2</sub> and 1T-TaS<sub>2</sub>, where large carrier concentration changes are responsible for the resistance jumps across phase transitions.

## 6. Electrically driven volatile threshold resistive switching

### 6.1 DC characterization

In addition to varying system temperature, adjacent phases in phase-change materials can be switched electrically either by local Joule heating or *via* electrical field effects. Such electrically controlled resistive switching holds unique advantages over other modulating parameters such as temperatures, high pressure, and optical pulses, owing to the relative ease of implementation in electronic devices. Depending on the inherent nature of the transition, these materials may exhibit volatile or non-volatile resistive switching. In this review, we focus on volatile threshold switching of these materials, although non-volatile multi-level resistive switching has also been reported under different testing conditions for both VO<sub>2</sub> and 1T-TaS<sub>2</sub>.<sup>46,110,127</sup>

VO<sub>2</sub> crystals and thin films undergo a structural and insulator-to-metal transitions upon heating to about 340 K, exhibiting a resistivity drop of several orders of magnitude, as shown in Figure 6a. Early research in the 1970s revealed resistive switching induced by applying voltage or current above a critical threshold, with negative differential resistance (NDR) commonly observed in current sweeping measurements (Figure 6b).<sup>128,129</sup> In 1980, Mansingh *et al.* systematically

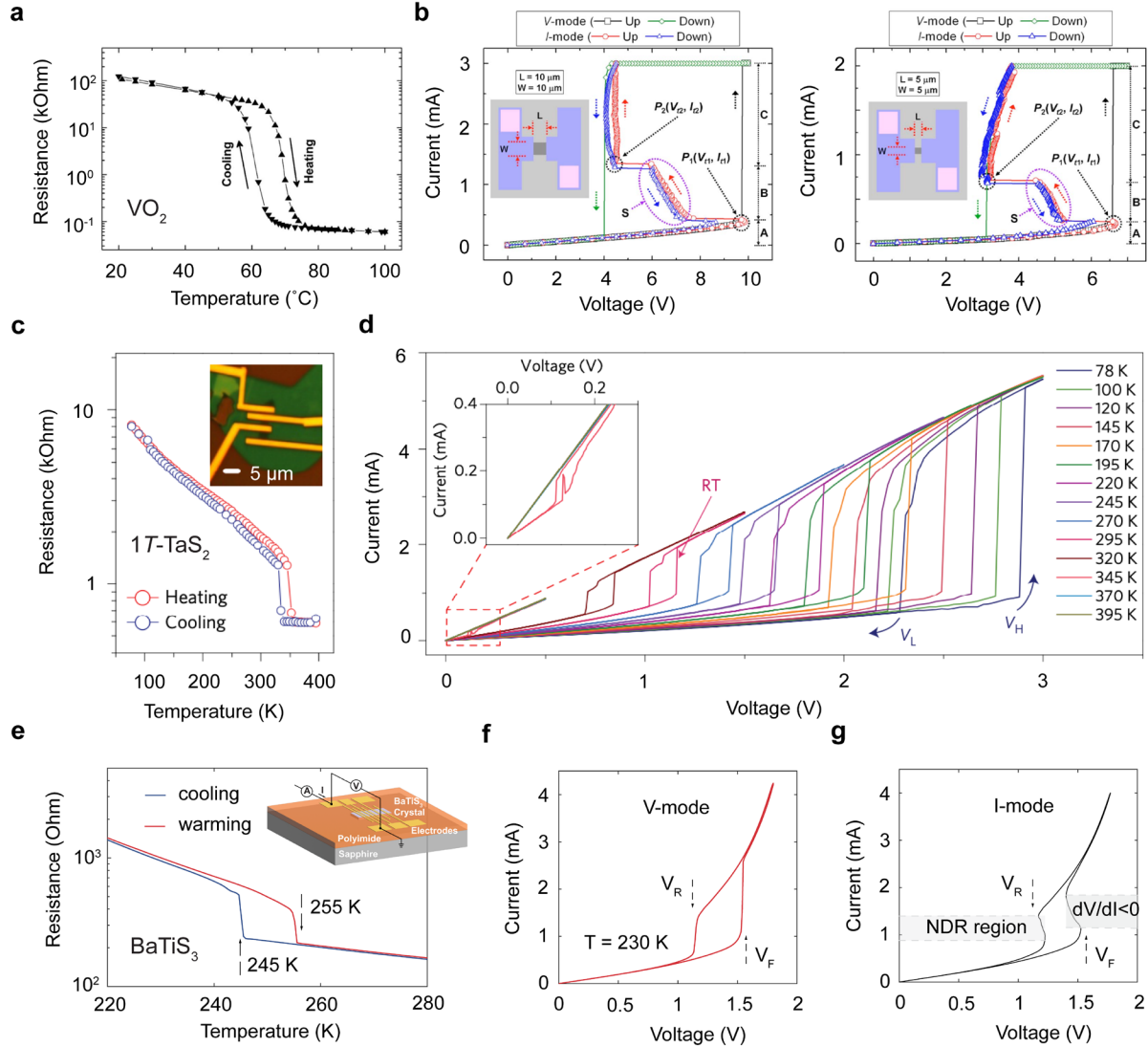


**Figure 6 DC-induced volatile threshold resistive switching.** (a) Temperature dependent resistances of a VO<sub>2</sub> thin film device from room temperature to 100°C. Figure adapted from Ref. [124] Copyright 2008, AIP Publishing. (b)  $I$ - $V$  characteristics of two VO<sub>2</sub> thin film devices with different active channel dimensions (10 μm × 10 μm, left; 5 μm × 5 μm, right) in both  $V$ -mode (voltage sweeps) and  $I$ -mode (current sweeps). Figure adapted from Ref. [104] Copyright 2010, AIP Publishing. (c) Temperature dependent resistances of a 9-nm-thick 1T-TaS<sub>2</sub> flake. The inset shows an optical microscopic image of a typical h-BN-capped 1T-TaS<sub>2</sub> device. (d) Temperature dependent  $I$ - $V$  characteristics of a thin flake 1T-TaS<sub>2</sub> device measured from 78 K to 395 K. (e) and (d) Figures adapted from Ref. [45] Copyright 2016, Springer Nature. (e) Temperature dependent resistance of a bulk BaTiS<sub>3</sub> device from 220 K to 280 K. The inset shows a schematic illustration of the planarized multi-terminal bulk device and the measurement circuit. (f) and (g) The corresponding  $I$ - $V$  characteristics at 230 K in both  $V$ -mode and  $I$ -mode. (e) to (g) Figures adapted from Ref. [34] Copyright 2023, John Wiley & Sons.

investigated the current-voltage ( $I$ - $V$ ) characteristics of a VO<sub>2</sub> single crystal between 220 K and

325 K, while tracking the crystal temperature through a thermocouple attached to the sample surface.<sup>32</sup> They observed that lowering the ambient temperature increased the threshold voltage ( $V_{th}$ ) upon switching but decreased the corresponding current ( $I_{th}$ ) at  $V_{th}$ , resulting in a nearly constant threshold power ( $V_{th} \times I_{th}$ ).<sup>32</sup> Notably, the measured crystal surface temperature rose only slightly above the ambient, remaining well below the bulk transition temperature of 340 K.<sup>32</sup> On this basis, they proposed a model involving a locally heated conducting channel of finite width, where switching is initiated once the channel temperature reaches the transition threshold of VO<sub>2</sub>.<sup>32</sup> More recently, Kumar *et al.* utilized black-body emission mapping to spatially resolved the temperature distribution of a VO<sub>2</sub> thin film under varying applied currents.<sup>130</sup> These results revealed the emergence and growth of a filament-shaped hot channel bridging the electrodes, further supporting the thermal nature of the switching.<sup>130</sup>

In 2015, Hollander *et al.* demonstrated electrically driven, reversible resistive switching between the insulating CCDW phase and metallic NCCDW/ICCDW phases in mechanically exfoliated 1T-TaS<sub>2</sub> flakes at cryogenic temperatures.<sup>33</sup> Both DC and pulsed voltages were employed to trigger abrupt insulator-to-metal transitions. Temperature-dependent  $I$ - $V$  characteristics revealed a constant threshold resistivity of approximately 7 mOhm-cm, which corresponded to a carrier concentration of about  $4.5 \times 10^{19} \text{ cm}^{-3}$ , consistent with that of the CCDW phase of 1T-TaS<sub>2</sub>.<sup>33</sup> In 2016, Liu *et al.* exploited the unique transport properties of ultrathin 1T-TaS<sub>2</sub> (6 to 9 nm in thickness), where the low-temperature insulator-to-metal transition between the CCDW and NCCDW phases is suppressed, to demonstrate volatile resistive switching devices based on the NCCDW-to-ICCDW transition, which operated at a wide temperature range from 78 K to 320 K,<sup>45</sup> as shown in Figure 6c and 6d. A room-temperature CDW oscillator was further constructed from these ultrathin 1T-TaS<sub>2</sub> devices, as discussed later in this review.

Reversible resistive switching in BaTiS<sub>3</sub> was first reported by Chen *et al.* in 2023, shortly after the initial discovery of phase transitions in this material.<sup>34</sup> BaTiS<sub>3</sub> exhibits a transition from a semiconducting room-temperature phase to a CDW state near 250 K, featuring a resistance jump of two- to threefold and a thermal hysteresis of  $\sim 10$  K,<sup>48</sup> as illustrated in Figure 6e. Structurally, this transition doubles the unit cell along the *a*- and *b*-axis with  $a = 2a_0$ ,  $b = 2b_0$ , and  $c = c_0$ . Electrically, BaTiS<sub>3</sub> exhibit a threshold switching behavior below its transition temperature ( $T_c$ ): the *I-V* characteristics show an abrupt switching to a conductive state above a threshold voltage ( $V_F$ ) during forward scan, and a return to its original high-resistance state below another critical voltage ( $V_R$ ) during reverse scan, forming a characteristic hysteresis window,<sup>34</sup> as shown in Figure 6f. When driving the device with a current source, an “S-type” NDR regime is also observed (Figure 6g).<sup>34</sup>

To assess the contribution of Joule heating in BaTiS<sub>3</sub> resistive switching, Chen *et al.* carried out four-probe *I-V* sweeps at various temperatures across the CDW transition.<sup>34</sup> They noted that the critical voltage ( $V_{th}$ ) required to switch the device increases with decreasing temperature, as does the threshold current ( $I_{th}$ ).<sup>34</sup> The threshold thermal power ( $P_{th}$ ) generated by Joule heating was then estimated using  $P_{th} = V_{th} \times I_{th}$  for both forward and reverse scans at each temperature. Unlike VO<sub>2</sub>, where  $P_{th}$  remains largely temperature-independent and hence the switching is achieved through a conducting channel (or filament),  $P_{th}$  in BaTiS<sub>3</sub> was found to decrease linearly as the temperature approached  $T_c$ . Two characteristic temperatures of 245 K and 258 K were extrapolated at which the threshold thermal power equals to zero, which aligns with the transition temperatures extracted from low-field transport measurements.<sup>34</sup> Based on these observations, Chen *et al.* suggested that the resistive switching in BaTiS<sub>3</sub> is primarily governed by local Joule

heating, which becomes substantial in their experimental scheme, considering the low thermal conductivity of both the BaTiS<sub>3</sub> crystal itself and the surrounding polymeric embedding medium.<sup>34</sup>

## 6.2 Pulsed $I$ - $V$ measurements

Pulsed  $I$ - $V$  measurements have emerged as a valuable electrical characterization technique for phase-change materials, offering two main advantages. First, they reduce the risk of device damages by mitigating excessive Joule heating; second, they provide insights into the switching mechanism by deconvoluting the thermal and electric-field contributions that can otherwise be conflated in conventional DC  $I$ - $V$  measurements. In a pulsed measurement, an arbitrary waveform generator produces a single or a series of pre-programmed voltage/current pulses and sends them to the device under test, while the response is recorded by an oscilloscope or other high-speed measurement instrument. A single square-shaped voltage pulse is typically defined by its width, period, rise/fall time, and amplitude; notably, the rise/fall times must be set significantly shorter than the pulse width to ensure a well-defined pulse waveform shape, and the extent of Joule heating is qualitatively tuned by adjusting the ration between the pulse width and pulse period.

In 2000, Stefanovich *et al.* employed back-gate pulses to inject electrons into a VO<sub>2</sub> film with a Si/SiO<sub>2</sub>/VO<sub>2</sub> device configuration, thereby inducing the semiconductor-to-metal transition by the increase of the electron density.<sup>60</sup> From this observation, they argued that the MIT in VO<sub>2</sub> is a purely Mott-Hubbard transition.<sup>60</sup> More recently, in 2019, Valle *et al.* investigated the dynamic response of VO<sub>2</sub> nanodevices under pulsed voltages.<sup>131</sup> As illustrated in Figure 7a, when the ambient temperature is below the critical temperature of ~330 K, the device remained in an insulating state for subthreshold pulsed voltages (< 1.6 V, 200 ns), yet became conducting for slightly higher pulses (~1.7 V).<sup>131</sup> Valle *et al.* further introduced an “electric transport pump-probe”

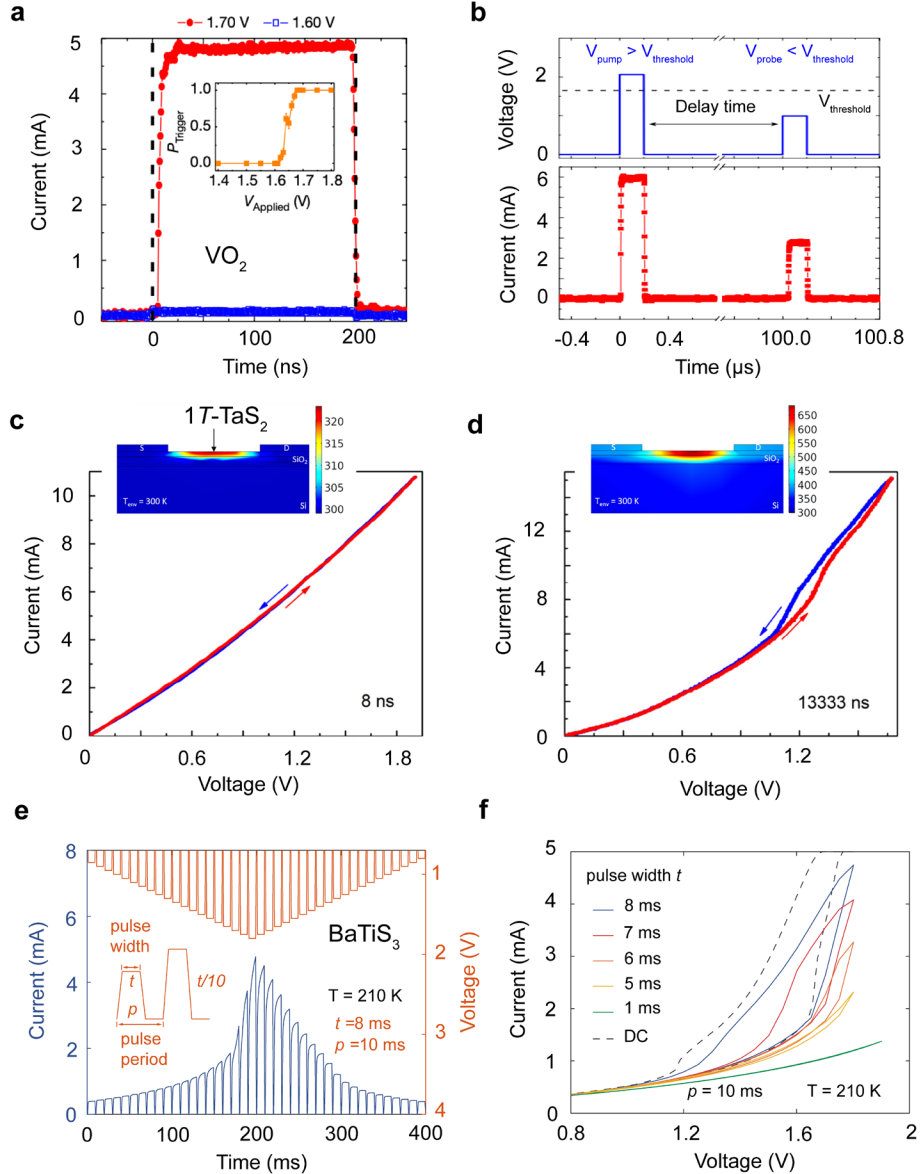


**Figure 7 Pulsed  $I$ - $V$  characterization.** (a) Time dependent current of a  $\text{VO}_2$  nanodevice at 330 K, in response to two voltage pulses (200 ns) with amplitudes of 1.6 V and 1.7 V. The inset shows the probability of triggering the IMT as a function of the pulse amplitude. (b) Illustration of the electrical transport pump-probe procedure and the corresponding current responses showing the  $\text{VO}_2$  device also being triggered by the subthreshold probe pulse. (a) and (b) Figures adapted from Ref. [131] Copyright 2019, Springer Nature. (c) and (d) Reconstructed  $I$ - $V$  characteristics of a  $1T\text{-TaS}_2$  flake device upon different pulse durations: 8 ns and 13333 ns. The inset shows the corresponding cross-sectional illustration of simulated temperature profiles near the device channel. Figures adapted from Ref. [133] Copyright 2021, AIP Publishing. (e) Pulsed  $I$ - $V$  characteristics of a two-terminal  $\text{BaTiS}_3$  device at 210 K. The pulse voltage was ramped from 0.8 V to 1.8 V. (f) Reconstructed  $I$ - $V$  characteristics of  $\text{BaTiS}_3$  from pulse measurements with pulse width varying from 8 to 1 ms while the pulse period was maintained at 10 ms. (e) and (f) Figures adapted from Ref. [34] Copyright 2023, John Wiley & Sons.

procedure to characterize the relaxation dynamics (Figure 7b). They used a 200 ns-wide “pump”



pulse ( $V_{\text{pump}} > V_{\text{th}}$ ) to drive the VO<sub>2</sub> into the metallic phase, followed by a second, subthreshold “probe” pulse ( $V_{\text{probe}} < V_{\text{th}}$ ) after a delay time  $\tau$ .<sup>131</sup> Surprisingly, even with  $V_{\text{pump}} = 1.25 V_{\text{th}}$ ,  $V_{\text{probe}} = 0.6 V_{\text{th}}$ , and a delay time  $\tau = 100 \mu\text{s}$  that is three orders of magnitude longer than the characteristic off delay ( $\sim 75 \text{ ns}$ ), the second subthreshold pulse still triggered the transition.<sup>131</sup> The authors attributed this to the intrinsic metastability of the first-order phase transition in VO<sub>2</sub>.<sup>131</sup>

Similarly, pulsed measurements have been extensively used to investigate the transport and resistive switching behavior of 1T-TaS<sub>2</sub>. In 1978, Uchida *et al.* studied nonlinear conduction in 1T-TaS<sub>2</sub> crystals using pulsed techniques, aiming to minimize sample self-heating.<sup>115</sup> They applied pulses of 2  $\mu\text{s}$  duration at a repetition frequency of 10 Hz, enabling electrical fields of up to 100 V/cm without significantly heating up the crystal.<sup>115</sup> In 2015, Vaskivskyi *et al.* employed 1- $\mu\text{s}$  current pulses to switch 1T-TaS<sub>2</sub> from its commensurate insulating CDW state to a metastable high-conductivity state, showing a well-defined threshold current and rapid switching dynamics ( $\sim 30 \text{ ps}$  rise/fall time).<sup>132</sup> More recently, in 2021, Mohammadzadeh *et al.* studied the NCCDW-to-ICCDW switching in exfoliated 1T-TaS<sub>2</sub> flakes using electrical pulses ranging from 8 ns to  $\sim 13 \mu\text{s}$ .<sup>133</sup> They found that the reconstructed pulsed  $I$ - $V$  characteristics exhibited no hysteresis for pulse durations below  $\sim 200 \text{ ns}$ , whereas longer pulses induced pronounced hysteresis that increased with pulse width.<sup>133</sup> Mohammadzadeh *et al.* further suggested that, despite the thermal origins of the switching, GHz-level switching speed are feasible in thin 1T-TaS<sub>2</sub> devices by optimizing device geometry and thermal resistance (Figure 7c and 7d).<sup>133</sup>

Turning to BaTiS<sub>3</sub>, pulsed  $I$ - $V$  measurements offer complementary evidence supporting the hypothesis of a Joule-heating-driven switching mechanism. Pulsed  $I$ - $V$  measurements were carried out on a two-terminal bulk BaTiS<sub>3</sub> device at 210 K with varying pulse widths ranging from 1 ms to 8 ms and a constant pulse period of 10 ms, as reported by Chen *et al.* in 2023.<sup>34</sup> As displayed in

Figure 7e, ramped voltage pulses with a width of 8 ms, leaving under 10% of the total cycle for cooling, were swept between 0.8 and 1.8 V and the current levels were recorded simultaneously. In this experimental scheme, the device exhibited a hysteretic switching behavior similar to that observed in DC measurements, as indicated by the asymmetric current profile.<sup>34</sup> Decreasing the pulse width from 8 ms to 1 ms, while maintaining the same voltage sweep ranges and pulse period, reduced the contribution of Joule heating and in turn narrowed the hysteresis window and raised the threshold switching voltage, as illustrated in Figure 7f.<sup>34</sup> Notably, no hysteresis was observed at 1 ms pulse width. Therefore, Chen *et al.* suggested that switching in BaTiS<sub>3</sub> is primarily thermally driven, as reducing pulse width decreases Joule heating power without altering the applied electric field.<sup>34</sup>

## 7. Self-sustaining voltage oscillations

Self-sustaining oscillations in VO<sub>2</sub> were first reported in 1975 by Taketa *et al.*, who employed a bulk crystal device (~ mm channel length) connected in series with a load resistor under an applied DC voltage,<sup>129</sup> as shown in Figure 8a. The oscillation frequency at room temperature was approximately 0.9 kHz, decreasing to 0.3 kHz at 55°C as the ambient temperature approached the transition temperature.<sup>129</sup> In 2008, Sakai *et al.* achieved a substantially higher oscillation frequency of ~ 550 kHz in a VO<sub>2</sub> thin-film device (10 μm × 10 μm × 0.22 μm), fabricated by PLD and subsequent dry etching.<sup>101</sup> Similar device performance with oscillation frequency > 0.5 MHz was demonstrated by Lee *et al.* on a sol-gel prepared VO<sub>2</sub> thin-film device with comparable lateral sizes (10 μm × 10 μm × 0.1 μm).<sup>134</sup> In 2011, Seo *et al.* experimentally investigated dimensional effects on VO<sub>2</sub> oscillators in planar device geometries, demonstrating a decrease in oscillation frequency as either the channel length or width increased (Figure 8b).<sup>135</sup> This finding suggests that

scaling the active device region could lead to higher oscillation frequencies, pending other limiting factors such as contact resistances or intrinsic capacitance.

In 2014, Beaumont *et al.* demonstrated oscillation frequencies of up to 300 kHz in out-of-plane VO<sub>2</sub> devices (3 μm × 3 μm) integrated in crossbars geometry.<sup>136</sup> They noted that such metal-VO<sub>2</sub>-metal configurations not only minimize the device footprint to enhance circuit integration, but also reduce the threshold voltage for triggering insulator-to-metal transition by shortening the conduction path to the film thickness (e.g., <100 nm).<sup>136</sup> However, using regular Ti/Au/Ti bottom electrodes largely constrained the achievable VO<sub>2</sub> film quality, likely due to limited growth temperatures or poor interfaces, resulting in low resistance jump across the MIT.<sup>136</sup> Similar limitations have been reported using SrRuO<sub>3</sub> or Pt bottom electrodes, where resistance changes across the transition are often below one order of magnitude.<sup>106</sup> In 2015, Mian *et al.* addresses these challenges by incorporating TiN as the bottom electrode, improving the interface and overall VO<sub>2</sub> film quality in an out-of-plane device configuration.<sup>105</sup> This approach yielded self-oscillations up to 9 MHz with low threshold switching voltages and currents.<sup>105</sup> Further optimization of thin-film deposition conditions and electrode-integration strategies, aimed at minimizing contact resistances and active channel sizes, could further increase the oscillation frequencies of VO<sub>2</sub> devices, thereby making them more attractive for practical applications.

Despite extensive research on bulk 1T-TaS<sub>2</sub> crystals in the 1970s and 1980s, including several studies on CDW-associated metal-insulator transitions,<sup>44,67</sup> the phase-change oscillator applications based on this material were not realized until the mid-2010s.<sup>45,47</sup> Much of the current electrical studies of 1T-TaS<sub>2</sub> relies on mechanically exfoliated microflakes, whose lateral dimensions and production yield remain limited. In 2016, Liu *et al.* constructed the first room-temperature CDW oscillator using thin 1T-TaS<sub>2</sub> flakes.<sup>45</sup> Their device exploits the electrically

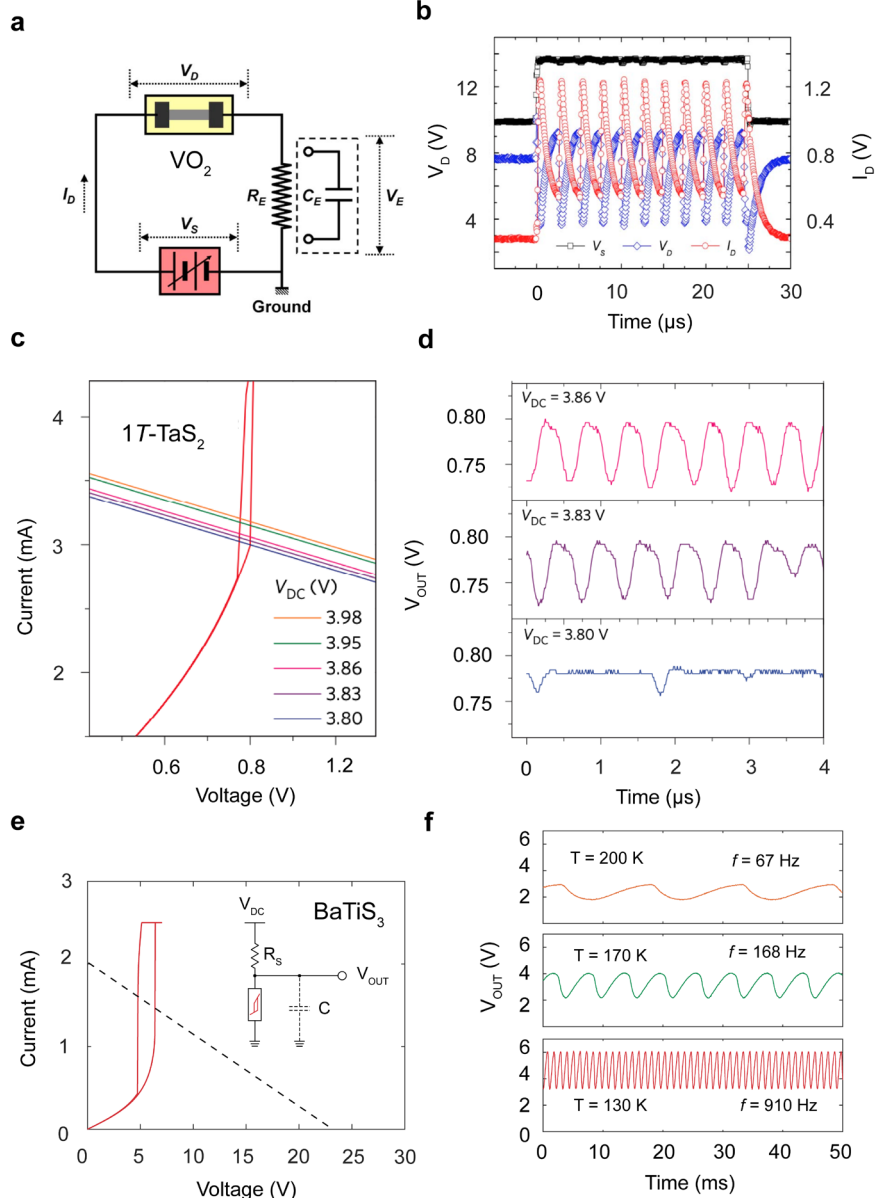


**Figure 8 Oscillator device performance.** (a) Schematic diagram of the electrical circuit used for the generation of the MIT oscillation in a  $\text{VO}_2$  thin film device. (b) Waveform of  $V_D$  and  $I_D$  of the device measured at room temperature. (a) and (b) Figure adapted from Ref. [104] Copyright 2010, AIP Publishing. (c)  $I$ - $V$  characteristics of a  $1T\text{-TaS}_2$  flake device at room temperature and load lines of the series resistor at different  $V_{DC}$  values. The oscillator circuit starts to oscillate across the threshold condition of  $V_{DC} = 3.8\text{ V}$ . (d) Voltage oscillations of a  $1T\text{-TaS}_2$  flake device under different  $V_{DC}$  values. (c) and (d) Figures adapted from Ref. [45] Copyright 2016, Springer Nature. (e)  $I$ - $V$  characteristics of a two-terminal  $\text{BaTiS}_3$  device at 220 K. The dashed line represents a series resistor load line for stable voltage oscillations and the inset shows a schematic illustration of the oscillator measurement circuit. (f) Oscillation waveforms of a  $\text{BaTiS}_3$  device operated at different temperatures. (e) and (f) Figures adapted from Ref. [34] Copyright 2023, John Wiley & Sons.

driven NCCDW-to-ICCDW transition near 350 K, achieving a maximum oscillation frequency of

~2 MHz in a simple oscillation circuit composed of a two-terminal 1T-TaS<sub>2</sub> device in series with a load resistor,<sup>45</sup> as shown in Figure 8c and 8d. They further integrated a top-gated graphene field-effect transistor (FET) with the 1T-TaS<sub>2</sub> device, enabling tunable oscillation frequencies through gate-mediated adjustments of the load resistance.<sup>45</sup> Although the 1T-TaS<sub>2</sub> flakes used for demonstration were only 6–9 nm thick, the same room-temperature oscillation behavior could, in principle, be observed in thicker 1T-TaS<sub>2</sub> crystals, provided that the NCCDW-to-ICCDW transition persists. Suppressing the low-temperature CCDW-to-NCCDW transition in such thin 1T-TaS<sub>2</sub> extends the oscillator's operation window to much lower temperature ranges without interference from the low-temperature transition. This disappearance of the CCDW-to-NCCDW transition in sufficiently thin 1T-TaS<sub>2</sub> flakes is typically attributed to extrinsic surface oxidation effects, as discussed by Tsen *et al.* in 2015.<sup>111</sup> Furthermore, Zhu *et al.* developed light-tunable CDW oscillators based on 1T-TaS<sub>2</sub>, whose oscillation frequency can be well modulated by varying the illumination intensity through the laser thermal effect.<sup>47</sup>

As discussed earlier, phase-change oscillators have been experimentally demonstrated in both VO<sub>2</sub> and 1T-TaS<sub>2</sub> with oscillation frequencies reaching the MHz regime, although the underlying switching mechanisms may differ. BaTiS<sub>3</sub> undergoes a unique semiconductor-to-CDW transition near 250 K, resulting in a two- to threefold resistivity jump and a thermal hysteresis window of ~ 10 K.<sup>34,48</sup> The overall shape of this transition, in terms of temperature-dependent resistivity, resembles that of the MIT in VO<sub>2</sub> or the ICCDW-to-NCCDW transition in 1T-TaS<sub>2</sub>, suggesting the feasibility of inducing voltage oscillations in BaTiS<sub>3</sub>. In 2023, Chen *et al.* reported the first phase-change oscillator based on single-crystal BaTiS<sub>3</sub> operating at 220 K (~ 30 K below its transition temperature), achieving an oscillation frequency of ~16 Hz by connecting a two-terminal BaTiS<sub>3</sub> device in series with a load resistor ( $R_s$ ) under a DC bias,<sup>34</sup> as shown in Figure

8e. The oscillation arises from volatile threshold resistive switching, a common feature of all three phase-change materials discussed here, and reflects the periodic changes of electrical resistance triggered by repetitive local heating and cooling cycles across the phase transition boundary.<sup>34</sup> When the voltage applied across the BaTiS<sub>3</sub> channel exceeds the critical voltage ( $V_F$ ), a transition to the low-resistance state is initiated due to Joule heating ( $P = \frac{V_{DC}^2}{(R+R_S)^2/R}$ ), resulting in a sudden increase in current and a subsequent increase in voltage across the load resistor<sup>34</sup>. The Joule heating power ( $P$ ) is insufficient to maintain the temperature in the low-resistance regime, because  $P$  decrease as  $R$  is reduced (for  $R < R_S$ ), driving BaTiS<sub>3</sub> back to the CDW state. The cycle repeats and yields self-sustaining voltage oscillations.<sup>34</sup>

Despite this successful demonstration in a relatively new phase-change material, the oscillation frequencies of BaTiS<sub>3</sub> single-crystal devices remain orders of magnitude lower than those reported for VO<sub>2</sub> and 1T-TaS<sub>2</sub>, due to combined effects of non-ideal sample morphologies, device geometries, and thermal managements.<sup>34</sup> Inspired by earlier efforts with VO<sub>2</sub> single-crystal oscillators,<sup>129</sup> Chen *et al.* employed a thermal management strategy to enhance the oscillation frequencies of BaTiS<sub>3</sub> devices.<sup>34</sup> Figure 8f shows that the oscillation frequency of the same device increased from 67 Hz to 910 Hz by lowering the operating temperature from 200 K to 130 K, benefited from an enhanced cooling efficiency.<sup>34</sup> However, maintaining stable CDW oscillations below  $\sim 130$  K proved challenging, as the low-temperature structural transition in BaTiS<sub>3</sub> starts to interfere with the switching behavior.<sup>48</sup> Strategies that can suppress this low-temperature transition could potentially improve the device performance but require further research investigations. Additionally, Chen *et al.* improved oscillation frequency by reducing the channel length, a method previously validated in other oscillating systems such as VO<sub>2</sub>.<sup>135</sup> Both operating at 170 K, a BaTiS<sub>3</sub> device with a 5  $\mu\text{m}$  channel outperformed a 10  $\mu\text{m}$  device by over a factor of three in oscillation

frequency.<sup>34</sup> This effect likely stems from more efficient local heating and cooling in smaller channels. Further reduction of the BaTiS<sub>3</sub> channel dimensions, including thickness, is expected to oscillation frequency significantly. Consequently, synthesizing high-quality BaTiS<sub>3</sub> thin film with intrinsic phase-change properties would be highly desired for their practical electronic device applications, benefiting from the precise thickness control and the fabrication scalability.

## **8. Neuron-like dynamics and higher-order complexity**

Large-scale transistor-based circuits, such as CPUs and GPUs, are now widely used to emulate biological dynamics and complexities.<sup>12,13</sup> However, as the task complexity grows, power consumption and associated device cooling requirements become increasingly restrictive. Alternatively, researchers seek to exploit novel materials and devices with intrinsic higher-order dynamics, realized through their internal electrophysical processes, to enable next-generation computing architectures that combine high computational capability with improved energy efficiency.

Volatile devices exhibiting threshold resistive switching are often capable of generating neuron-like temporal dynamics of higher-order complexity, making them excellent candidates for artificial neuron applications. According to Kumar *et al.*'s classification of neuronal devices, most selector-type devices with volatile threshold switching and relatively simple dynamics are categorized as first-order.<sup>137</sup> This class includes the two-terminal VO<sub>2</sub>, 1T-TaS<sub>2</sub>, and BaTiS<sub>3</sub> devices discussed herein, even though the underlying operating mechanisms (e.g., MIT, CDW, or Mott) may vary. Second-order neuronal complexity, often arising from self-sustaining oscillations, can be realized by integrating a first-order device into a relaxation oscillator circuit with typically a parallel capacitor and a series resistor.<sup>137</sup> Standalone second-order devices are also possible when

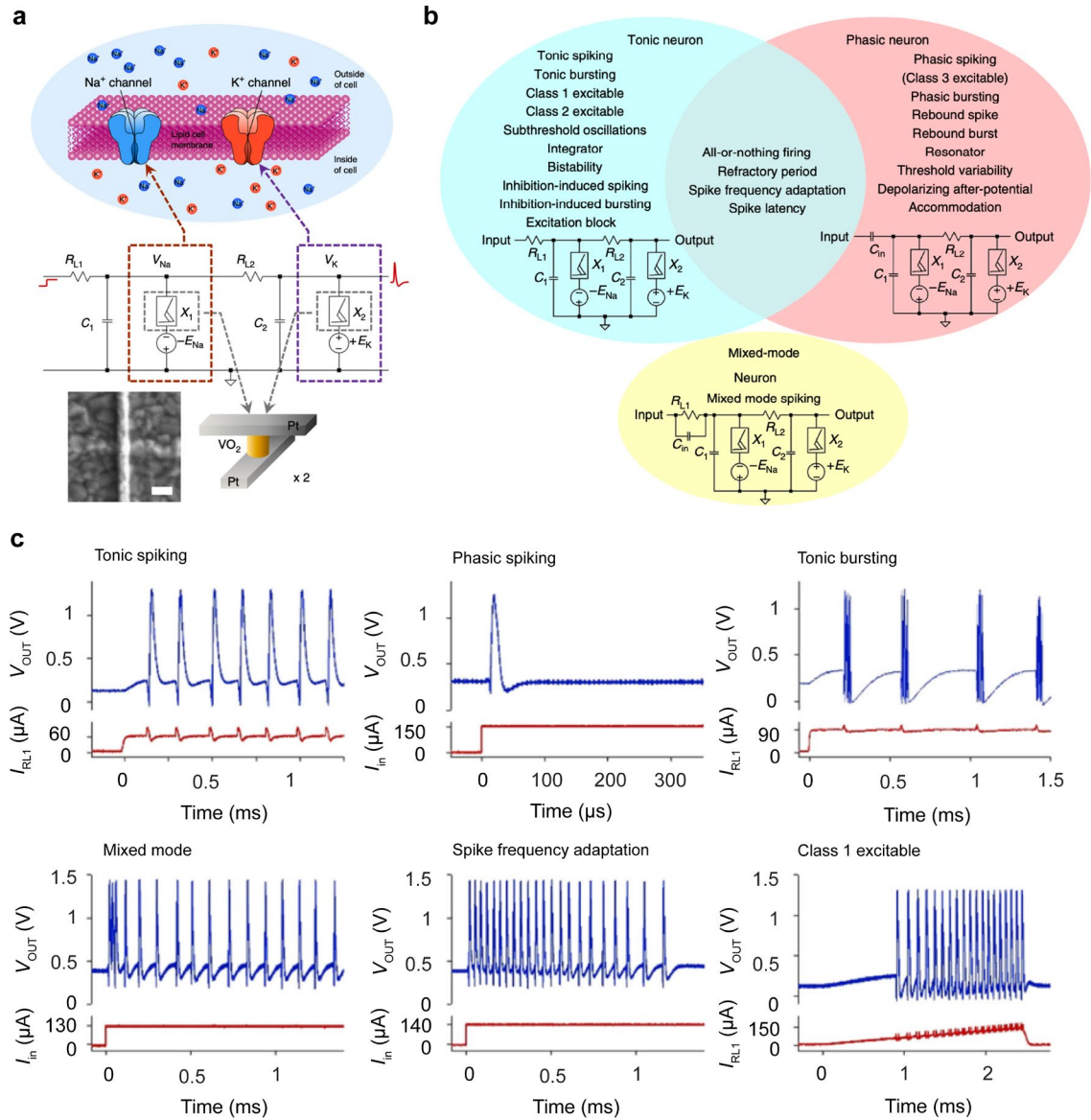


**Figure 9 Neuron-like dynamics and higher-order complexity.** (a) Representative biological neuron spiking behaviors experimentally demonstrated in single VO<sub>2</sub> active memristor neurons, including tonic spiking, phasic spiking, tonic bursting, mixed mode, spike frequency adaptation, and class 1 excitable. The demonstration of a full list of 23 neuron spiking behaviors can be found in Ref. (b) 20  $I$ - $V$  curves of a 1T-TaS<sub>2</sub> device measured under same conditions. The threshold voltage  $V_{th}$  of the transitions vary cycle-to-cycle from 0.823 V to 0.840 V. (c) A typical series of waveforms excited in a 1T-TaS<sub>2</sub> artificial neuron by increasing  $V_{DC}$ . (a) to (c) Figures adapted from Ref. [139] Copyright 2018, Springer Nature.

their built-in capacitance is sufficiently large to sustain the oscillations without the need for an external parallel capacitor, as demonstrated with NbO<sub>2</sub>.<sup>138</sup>



Achieving even higher-order complexities often requires multiple coupled circuit elements. For instance, Yi *et al.* reported a non-transistor fourth-order neuronal system employing two volatile first-order VO<sub>2</sub> devices to emulate the biologically accurate Hodgkin-Huxley neuron model model.<sup>139</sup> This approach successfully reproduced all 23 neuronal functionalities, including spiking, bursting and mixed mode firing. Figure 9a illustrates the structure of a biological neuron membrane, highlighting Na<sup>+</sup> and K<sup>+</sup> channels. In the corresponding circuit diagram, two VO<sub>2</sub> neuronal devices (X<sub>1</sub> and X<sub>2</sub>) are coupled with two capacitors (C<sub>1</sub> and C<sub>2</sub>) and two series load resistors (R<sub>L1</sub> and R<sub>L2</sub>). When driven by a steady DC current, this circuit can produce periodic bursts of spikes, a hallmark of tonically active neurons.<sup>139</sup> By either replacing the load resistor R<sub>L1</sub> with a capacitor C<sub>in</sub>, or by inserting C<sub>in</sub> before R<sub>L1</sub> in the tonic neuron circuit, one can emulate another basic type of neurons, i.e., phasically active neurons, characterized by a single spike fired upon the onset of a DC input followed by quiescence afterwards.<sup>139</sup> Moreover, by placing a capacitor C<sub>in</sub> in parallel with R<sub>L1</sub>, a mixed-mode neuron can be simulated, which features a phasic burst followed by a series of tonic spiking upon applying the DC input. Figure 9b shows circuit schematics for these three basic prototype neurons and the corresponding 23 experimentally demonstrated biological neuron spiking behaviors, part of which are illustrated in Figure 9c. A detailed circuit design and neuron emulation results can be found in the original reference.<sup>139</sup>

Analogous to VO<sub>2</sub>, first-order 1T-TaS<sub>2</sub> and BaTiS<sub>3</sub> neuronal devices also offer promise for constructing higher-order neuron circuits, considering their demonstrated volatile threshold switching and oscillatory behaviors. However, whereas high-quality thin-film synthesis and large-scale device integration of VO<sub>2</sub> are relatively well established, the scalable fabrication of 1T-TaS<sub>2</sub> microflakes and BaTiS<sub>3</sub> bulk crystals remains challenging. Advancing the synthesis of 1T-TaS<sub>2</sub>

and BaTiS<sub>3</sub> thin films with pristine CDW phase transitions is thus essential to unlock energy-efficient, chalcogenide-based neuronal device applications in the future.

## 9. Summary and outlook

Here, we have reviewed recent research progresses on archetypal phase-change materials exhibiting MIT or CDW behavior—specifically, the correlated oxide VO<sub>2</sub>, the transition metal dichalcogenide 1T-TaS<sub>2</sub>, and the hexagonal chalcogenide perovskite BaTiS<sub>3</sub>—and their applications in neuronal devices. Despite differences in chemical composition, morphology, and underlying phase-change mechanisms, these three materials display similar volatile threshold resistive switching across the associated transitions and exhibit self-sustaining voltage oscillations, making them promising candidates for neuronal devices. From the perspective of materials development, we discussed their structural phase transitions, synthesis methods, and contact fabrication processes. In addition, we surveyed their electrical transport properties, basic switching device characterization, under both DC and pulsed operations, and their integration into neuronal circuits to emulate complex biological neuronal behaviors.

Despite these advances, there are still significant challenges for practical implementation of these volatile switching-based phase-change neurons in neuromorphic computing. For instance, to be compatible with the processing conditions for fabricating artificial synapses or CMOS-based chips, the material deposition temperature must be maintained below 400°C, or alternative heterogeneous integration approaches must be developed. Among these three materials, VO<sub>2</sub> is currently the only system demonstrating high-quality thin-film deposition processes that produce an MIT transition comparable to that of a bulk crystals.<sup>86</sup> However, deposition at such reduced

temperatures compromised materials quality, reducing the amplitude of the resistance jump and narrowing the operational window for neuronal oscillations.

Even more research efforts are required for the two CDW-based materials, i.e.,  $1T$ -TaS<sub>2</sub> and BaTiS<sub>3</sub>. So far, single crystals of  $1T$ -TaS<sub>2</sub> and BaTiS<sub>3</sub> are still being used to examine their intrinsic material properties and demonstrate proof-of-concept prototype devices. Although several back-end-of-line (BEOL)-compatible 2D and 3D integration approaches have been recently reported,<sup>140-142</sup> such labor-intense integration procedures and limited device packing density would inevitably increase the overall fabrication cost when dealing with  $1T$ -TaS<sub>2</sub> and BaTiS<sub>3</sub>. Developing high-quality thin-film synthesis approaches for these materials is itself a demanding but rather challenging task, considering the susceptibility of external factors such as strain, defects, and doping on CDW phase transitions. Alternatively, one may also leverage this sensitivity to intentionally tune the phase transition temperatures as needed and to maximize the overall device performance.

## **Author declarations**

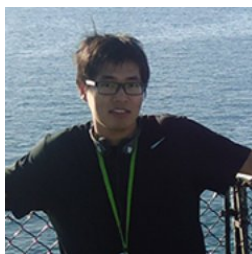
## **Acknowledgements**

We gratefully acknowledge support from an ARO MURI program (W911NF-21-1-0327), an ARO grant (W911NF-19-1-0137) and National Science Foundation (DMR-2122071).

## **Conflict of interest**

The authors declare no competing financial interests.

## Biographies



**Huandong Chen** is currently a postdoctoral researcher in Condensed Matter Physics and Materials Science Department at Brookhaven National Laboratory, working on low-dimensional quantum materials and devices using Scanning Tunneling Microscopy (STM). He received his Ph.D. degree in Materials Science from University of Southern California in 2023, where he has worked on bulk single crystal synthesis, transport studies and electronic and optoelectronic devices of novel complex chalcogenides.



**Jayakanth Ravichandran** is currently a Professor of Chemical Engineering and Materials Science and Electrical and Computer Engineering at University of Southern California, and the holder of the Philip and Cayley MacDonald Endowed Early Career Chair. He is also a co-director of the Core Center for Excellence in Nano Imaging. He completed his graduate work at University of California, Berkley in Applied Science and Technology, and postdoc in Physics at Columbia

University and Harvard University. His research interests are in the broad area of electronic and photonic materials and devices.

## References

- 1 Leiserson, C. E. *et al.* There's plenty of room at the Top: What will drive computer performance after Moore's law? *Science* **368**, eaam9744 (2020).
- 2 Shalf, J. The future of computing beyond Moore's Law. *Philosophical Transactions of the Royal Society A* **378**, 20190061 (2020).
- 3 Wang, H. *et al.* Scientific discovery in the age of artificial intelligence. *Nature* **620**, 47-60 (2023).
- 4 Jeong, D. S. *et al.* Memristors for energy-efficient new computing paradigms. *Advanced Electronic Materials* **2**, 1600090 (2016).
- 5 Choi, S. *et al.* Emerging memristive artificial synapses and neurons for energy-efficient neuromorphic computing. *Adv. Mater.* **32**, 2004659 (2020).
- 6 Zhang, W. *et al.* Neuro-inspired computing chips. *Nat. Electron.* **3**, 371-382 (2020).
- 7 Ham, D. *et al.* Neuromorphic electronics based on copying and pasting the brain. *Nat. Electron.* **4**, 635-644 (2021).
- 8 Marković, D. *et al.* Physics for neuromorphic computing. *Nat. Rev. Phys.* **2**, 499-510 (2020).
- 9 Ielmini, D. & Wong, H.-S. P. In-memory computing with resistive switching devices. *Nat. Electron.* **1**, 333-343 (2018).
- 10 Tang, J. *et al.* Bridging biological and artificial neural networks with emerging neuromorphic devices: fundamentals, progress, and challenges. *Adv. Mater.* **31**, 1902761 (2019).

- 11 Izhikevich, E. M. Which model to use for cortical spiking neurons? *IEEE transactions on neural networks* **15**, 1063-1070 (2004).
- 12 Prezioso, M. *et al.* Training and operation of an integrated neuromorphic network based on metal-oxide memristors. *Nature* **521**, 61-64 (2015).
- 13 Yao, P. *et al.* Fully hardware-implemented memristor convolutional neural network. *Nature* **577**, 641-646 (2020).
- 14 Yang, J. J. *et al.* Memristive devices for computing. *Nat. Nanotechnol.* **8**, 13-24 (2013).
- 15 Wang, Z. *et al.* Memristors with diffusive dynamics as synaptic emulators for neuromorphic computing. *Nat. Mater.* **16**, 101-108 (2017).
- 16 Shi, Y. *et al.* Electronic synapses made of layered two-dimensional materials. *Nat. Electron.* **1**, 458-465 (2018).
- 17 Sarwat, S. G. *et al.* Phase-change memtransistive synapses for mixed-plasticity neural computations. *Nat. Nanotechnol.* **17**, 507-513 (2022).
- 18 Wong, H.-S. P. *et al.* Phase change memory. *Proc. IEEE* **98**, 2201-2227 (2010).
- 19 Chanthbouala, A. *et al.* A ferroelectric memristor. *Nat. Mater.* **11**, 860-864 (2012).
- 20 Scott, J. F. & Paz de Araujo, C. A. Ferroelectric memories. *Science* **246**, 1400-1405 (1989).
- 21 Jerry, M. *et al.* in *2017 IEEE international electron devices meeting (IEDM)*. 6.2. 1-6.2. 4 (IEEE).
- 22 Ikeda, S. *et al.* Magnetic tunnel junctions for spintronic memories and beyond. *IEEE Trans. Electron Devices* **54**, 991-1002 (2007).
- 23 Krzysteczko, P. *et al.* The memristive magnetic tunnel junction as a nanoscopic synapse-neuron system. *Adv. Mater.* **24**, 762-766 (2012).

- 24 Thomas, A. *et al.* Tunnel junction based memristors as artificial synapses. *Frontiers in neuroscience* **9**, 241 (2015).
- 25 Yu, Y. *et al.* Electrical and thermal dynamics of self-oscillations in TaO<sub>x</sub>-based threshold switching devices. *ACS Appl. Electron. Mater.* **2**, 683-691 (2020).
- 26 Kim, T. *et al.* An artificial neuron using a bipolar electrochemical metallization switch and its enhanced spiking properties through filament confinement. *Advanced Electronic Materials* **7**, 2000410 (2021).
- 27 Wang, M. *et al.* S-type negative differential resistance in semiconducting transition-metal dichalcogenides. *Advanced Electronic Materials* **5**, 1800853 (2019).
- 28 Li, S. *et al.* Origin of current-controlled negative differential resistance modes and the emergence of composite characteristics with high complexity. *Adv. Funct. Mater.* **29**, 1905060 (2019).
- 29 Wang, Z. & Khan, A. I. Ferroelectric relaxation oscillators and spiking neurons. *IEEE Journal on Exploratory Solid-State Computational Devices and Circuits* **5**, 151-157 (2019).
- 30 Wang, Z. *et al.* Ferroelectric oscillators and their coupled networks. *IEEE Electron Device Lett.* **38**, 1614-1617 (2017).
- 31 Zhang, X. *et al.* An artificial spiking afferent nerve based on Mott memristors for neurorobotics. *Nat. Commun.* **11**, 51 (2020).
- 32 Mansingh, A. *et al.* Electrical switching in single crystal VO<sub>2</sub>. *Solid-State Electron.* **23**, 649-654 (1980).
- 33 Hollander, M. J. *et al.* Electrically driven reversible insulator–metal phase transition in 1T-TaS<sub>2</sub>. *Nano Lett.* **15**, 1861-1866 (2015).



- 34 Chen, H. *et al.* Charge-density-wave resistive switching and voltage oscillations in ternary chalcogenide BaTiS<sub>3</sub>. *Advanced Electronic Materials* **9**, 2300461 (2023).
- 35 Morin, F. Oxides which show a metal-to-insulator transition at the Neel temperature. *Phys. Rev. Lett.* **3**, 34 (1959).
- 36 Sakata, K. Note on the phase transition in NbO<sub>2</sub>. *J. Phys. Soc. Jpn.* **26**, 582-582 (1969).
- 37 Shapiro, S. *et al.* Neutron scattering study of the structural phase transition in NbO<sub>2</sub>. *Solid State Commun.* **15**, 377-381 (1974).
- 38 Torrance, J. *et al.* Systematic study of insulator-metal transitions in perovskites RNiO<sub>3</sub> (R= Pr, Nd, Sm, Eu) due to closing of charge-transfer gap. *Phys. Rev. B* **45**, 8209 (1992).
- 39 Torriss, B. *et al.* Metal-insulator transition of strained SmNiO<sub>3</sub> thin films: Structural, electrical and optical properties. *Scientific reports* **7**, 40915 (2017).
- 40 Qazilbash, M. M. *et al.* Mott transition in VO<sub>2</sub> revealed by infrared spectroscopy and nano-imaging. *Science* **318**, 1750-1753 (2007).
- 41 Mott, N. *Metal-insulator transitions*. (CRC Press, 2004).
- 42 Imada, M. *et al.* Metal-insulator transitions. *Rev. Mod. Phys.* **70**, 1039 (1998).
- 43 Zhu, X. *et al.* Misconceptions associated with the origin of charge density waves. *Adv. Phys.: X* **2**, 622-640 (2017).
- 44 Thompson, A. *et al.* Transitions between semiconducting and metallic phases in 1-T TaS<sub>2</sub>. *Solid State Commun.* **9**, 981-985 (1971).
- 45 Liu, G. *et al.* A charge-density-wave oscillator based on an integrated tantalum disulfide–boron nitride–graphene device operating at room temperature. *Nat. Nanotechnol.* **11**, 845-850 (2016).

- 46 Yoshida, M. *et al.* Memristive phase switching in two-dimensional 1T-TaS<sub>2</sub> crystals. *Sci. Adv.* **1**, e1500606 (2015).
- 47 Zhu, C. *et al.* Light-tunable 1T-TaS<sub>2</sub> charge-density-wave oscillators. *ACS Nano* **12**, 11203-11210 (2018).
- 48 Chen, H. *et al.* Charge density wave order and electronic phase transitions in a dilute *d*-band semiconductor. *Adv. Mater.* **35**, 2303283 (2023).
- 49 Wu, D. *et al.* Layered semiconductor EuTe<sub>4</sub> with charge density wave order in square tellurium sheets. *Phys. Rev. Mater.* **3**, 024002 (2019).
- 50 Venturini, R. *et al.* Electrically driven non-volatile resistance switching between charge density wave states at room temperature. *arXiv preprint arXiv:2412.13094* (2024).
- 51 Schofield, P. *et al.* Harnessing the metal–insulator transition of VO<sub>2</sub> in neuromorphic computing. *Adv. Mater.* **35**, 2205294 (2023).
- 52 Liu, H. *et al.* Artificial neuronal devices based on emerging materials: neuronal dynamics and applications. *Adv. Mater.* **35**, 2205047 (2023).
- 53 Yang, Z. *et al.* Oxide electronics utilizing ultrafast metal-insulator transitions. *Annu. Rev. Mater. Res.* **41**, 337-367 (2011).
- 54 Goodenough, J. B. The two components of the crystallographic transition in VO<sub>2</sub>. *J. Solid State Chem.* **3**, 490-500 (1971).
- 55 Hearn, C. Phonon softening and the metal-insulator transition in VO<sub>2</sub>. *J. Phys. C: Solid State Phys.* **5**, 1317 (1972).
- 56 Scruby, C. *et al.* The role of charge density waves in structural transformations of 1T-TaS<sub>2</sub>. *Philos. Mag.* **31**, 255-274 (1975).
- 57 Peierls, R. & Peierls, R. E. *Quantum theory of solids*. (Oxford University Press, 1955).

- 58 Grüner, G. The dynamics of charge-density waves. *Rev. Mod. Phys.* **60**, 1129 (1988).
- 59 Zylbersztejn, A. & Mott, N. F. Metal-insulator transition in vanadium dioxide. *Phys. Rev. B* **11**, 4383 (1975).
- 60 Stefanovich, G. *et al.* Electrical switching and Mott transition in VO<sub>2</sub>. *J. Phys.: Condens. Matter* **12**, 8837 (2000).
- 61 Morrison, V. R. *et al.* A photoinduced metal-like phase of monoclinic VO<sub>2</sub> revealed by ultrafast electron diffraction. *Science* **346**, 445-448 (2014).
- 62 Biermann, S. *et al.* Dynamical singlets and correlation-assisted Peierls transition in VO<sub>2</sub>. *Phys. Rev. Lett.* **94**, 026404 (2005).
- 63 Rossnagel, K. On the origin of charge-density waves in select layered transition-metal dichalcogenides. *J. Phys.: Condens. Matter* **23**, 213001 (2011).
- 64 Wilson, J. A. & Yoffe, A. The transition metal dichalcogenides discussion and interpretation of the observed optical, electrical and structural properties. *Adv. Phys.* **18**, 193-335 (1969).
- 65 Williams, P. *et al.* Diffraction evidence for the Kohn anomaly in 1T-TaS<sub>2</sub>. *Philos. Mag.* **29**, 695-699 (1974).
- 66 Fazekas, P. & Tosatti, E. Electrical, structural and magnetic properties of pure and doped 1T-TaS<sub>2</sub>. *Philos. Mag. B* **39**, 229-244 (1979).
- 67 Inada, R. *et al.* Hall effect of 1T-TaS<sub>2</sub>. *Phys. Lett. A* **69**, 453-456 (1979).
- 68 Inada, R. *et al.* Hall effect of 1T-TaS<sub>2</sub> and 1T-TaSe<sub>2</sub>. *Physica B+ C* **99**, 188-192 (1980).
- 69 Niu, S. *et al.* Giant optical anisotropy in a quasi-one-dimensional crystal. *Nat. Photonics* **12**, 392-396 (2018).
- 70 Fagot, S. *et al.* One-dimensional instability in BaVS<sub>3</sub>. *Phys. Rev. Lett.* **90**, 196401 (2003).

- 71 Inami, T. *et al.* Symmetry breaking in the metal-insulator transition of BaVS<sub>3</sub>. *Phys. Rev. B* **66**, 073108 (2002).
- 72 Laudise, R. & Nielsen, J. in *Solid State Phys.* Vol. 12 149-222 (Elsevier, 1961).
- 73 Ladd, L. A. & Paul, W. Optical and transport properties of high quality crystals of V<sub>2</sub>O<sub>4</sub> near the metallic transition temperature. *Solid State Commun.* **7**, 425-428 (1969).
- 74 Schmidt, P. *et al.* Chemical vapor transport reactions—methods, materials, modeling. *Advanced Topics on Crystal Growth*, 227-305 (2013).
- 75 Nagasawa, K. Crystal growth of V<sub>n</sub>O<sub>2n-1</sub> (3 ≤ n ≤ 8) by the chemical transport reaction and electrical properties. *Mater. Res. Bull.* **6**, 853-863 (1971).
- 76 Reyes, J. *et al.* Electrical, optical, magnetic resonance and microhardness properties of tungsten-doped VO<sub>2</sub>. *J. Can. Ceram. Soc* **41**, 1-8 (1972).
- 77 Schäfer, H. *Chemical transport reactions.* (Elsevier, 2013).
- 78 Yu, Y. *et al.* Gate-tunable phase transitions in thin flakes of 1T-TaS<sub>2</sub>. *Nat. Nanotechnol.* **10**, 270-276 (2015).
- 79 Hahn, H. & Mutschke, U. Untersuchungen über ternäre chalcogenide. XI. versuche zur darstellung von thioperowskiten. *Z. Anorg. Allg. Chem.* **288**, 269-278 (1957).
- 80 Imai, H. *et al.* Calorimetric Study on Metal-Insulator Transition of Quasi-One-Dimensional BaVS<sub>3</sub>. *J. Phys. Soc. Jpn.* **65**, 3460-3463 (1996).
- 81 Yang, F. *et al.* Strongly anisotropic quasi-1D BaTiS<sub>3</sub> chalcogenide perovskite for near-infrared polarized photodetection. *Adv. Opt. Mater.* **11**, 2201859 (2022).
- 82 Zhao, B. *et al.* Orientation-controlled anisotropy in single crystals of quasi-1D BaTiS<sub>3</sub>. *Chem. Mater.* **34**, 5680-5689 (2022).

- 83 Chen, H. *et al.* Molten flux growth of single crystals of quasi-1D hexagonal chalcogenide BaTiS<sub>3</sub>. *J. Mater. Res.* **39**, 1901-1910 (2024).
- 84 Fuls, E. *et al.* Reactively sputtered vanadium dioxide thin films. *Appl. Phys. Lett.* **10**, 199-201 (1967).
- 85 Hensler, D. Transport properties of sputtered vanadium dioxide thin films. *J. Appl. Phys.* **39**, 2354-2360 (1968).
- 86 Kim, D. & Kwok, H. S. Pulsed laser deposition of VO<sub>2</sub> thin films. *Appl. Phys. Lett.* **65**, 3188-3190 (1994).
- 87 Sakai, J. *et al.* Pulsed laser-deposited VO<sub>2</sub> thin films on Pt layers. *J. Appl. Phys.* **113**, 123503 (2013).
- 88 Borek, M. *et al.* Pulsed laser deposition of oriented VO<sub>2</sub> thin films on R-cut sapphire substrates. *Appl. Phys. Lett.* **63**, 3288-3290 (1993).
- 89 Shepelin, N. A. *et al.* A practical guide to pulsed laser deposition. *Chem. Soc. Rev.* (2023).
- 90 Paik, H. *et al.* Transport properties of ultra-thin VO<sub>2</sub> films on (001) TiO<sub>2</sub> grown by reactive molecular-beam epitaxy. *Appl. Phys. Lett.* **107**, 163101 (2015).
- 91 Fan, L. *et al.* Infrared response and optoelectronic memory device fabrication based on epitaxial VO<sub>2</sub> film. *ACS Appl. Mater. Interfaces* **8**, 32971-32977 (2016).
- 92 Chang, H. *et al.* Epitaxial TiO<sub>2</sub> and VO<sub>2</sub> films prepared by MOCVD. *Appl. Surf. Sci.* **48**, 12-18 (1991).
- 93 Chae, B.-G. *et al.* Highly oriented VO<sub>2</sub> thin films prepared by sol-gel deposition. *Electrochem. Solid-State Lett.* **9**, C12 (2005).

- 94 Wang, N. *et al.* Simple sol–gel process and one-step annealing of vanadium dioxide thin films: synthesis and thermochromic properties. *Thin Solid Films* **534**, 594-598 (2013).
- 95 Zhang, H.-T. *et al.* Wafer-scale growth of VO<sub>2</sub> thin films using a combinatorial approach. *Nat. Commun.* **6**, 1-8 (2015).
- 96 Fu, W. *et al.* Controlled synthesis of atomically thin 1T-TaS<sub>2</sub> for tunable charge density wave phase transitions. *Chem. Mater.* **28**, 7613-7618 (2016).
- 97 Lin, H. *et al.* Growth of atomically thick transition metal sulfide films on graphene / 6H-SiC (0001) by molecular beam epitaxy. *Nano Research* **11**, 4722-4727 (2018).
- 98 Surendran, M. *et al.* Quasi-epitaxial growth of BaTiS<sub>3</sub> films. *J. Mater. Res.* **37**, 3481-3490 (2022).
- 99 Surendran, M. *et al.* A hybrid pulsed laser deposition approach to grow thin films of chalcogenides. *Adv. Mater.* **36**, 2312620 (2024).
- 100 Surendran, M. *et al.* Epitaxial thin films of a chalcogenide perovskite. *Chem. Mater.* **33**, 7457-7464 (2021).
- 101 Sakai, J. High-efficiency voltage oscillation in VO<sub>2</sub> planer-type junctions with infinite negative differential resistance. *J. Appl. Phys.* **103**, 103708 (2008).
- 102 Ham, Y.-H. *et al.* Etching characteristics of VO<sub>2</sub> thin films using inductively coupled Cl<sub>2</sub>/Ar plasma. *Jpn. J. Appl. Phys.* **48**, 08HD04 (2009).
- 103 Ruzmetov, D. *et al.* Three-terminal field effect devices utilizing thin film vanadium oxide as the channel layer. *J. Appl. Phys.* **107**, 114516 (2010).
- 104 Kim, H. T. *et al.* Electrical oscillations induced by the metal-insulator transition in VO<sub>2</sub>. *J. Appl. Phys.* **107**, 023702 (2010).

- 105 Mian, M. S. *et al.* Self-oscillation up to 9 MHz based on voltage triggered switching in VO<sub>2</sub>/TiN point contact junctions. *J. Appl. Phys.* **117**, 215305 (2015).
- 106 Zhang, C. *et al.* Synthesis and electrical behavior of VO<sub>2</sub> thin films grown on SrRuO<sub>3</sub> electrode layers. *Journal of Vacuum Science & Technology A* **40** (2022).
- 107 Frindt, R. & Yoffe, A. Physical properties of layer structures: optical properties and photoconductivity of thin crystals of molybdenum disulphide. *Proceedings of the Royal Society of London. Series A. Mathematical and Physical Sciences* **273**, 69-83 (1963).
- 108 Novoselov, K. S. *et al.* Electric field effect in atomically thin carbon films. *Science* **306**, 666-669 (2004).
- 109 Geim, A. K. Graphene: status and prospects. *Science* **324**, 1530-1534 (2009).
- 110 Patel, T. *et al.* Photocurrent imaging of multi-memristive charge density wave switching in two-dimensional 1T-TaS<sub>2</sub>. *Nano Lett.* **20**, 7200-7206 (2020).
- 111 Tsen, A. W. *et al.* Structure and control of charge density waves in two-dimensional 1T-TaS<sub>2</sub>. *Proc. Natl. Acad. Sci.* **112**, 15054-15059 (2015).
- 112 Li, Q. *et al.* Chiral magnetic effect in ZrTe<sub>5</sub>. *Nat. Phys.* **12**, 550-554 (2016).
- 113 Gooth, J. *et al.* Axionic charge-density wave in the Weyl semimetal (TaSe<sub>4</sub>)<sub>2</sub>I. *Nature* **575**, 315-319 (2019).
- 114 Chu, J.-H. *et al.* In-plane resistivity anisotropy in an underdoped iron arsenide superconductor. *Science* **329**, 824-826 (2010).
- 115 Uchida, S. *et al.* Nonlinear conduction in two-dimensional CDW system: 1T-TaS<sub>2</sub>. *Solid State Commun.* **27**, 637-640 (1978).
- 116 Kang, D. *et al.* Printed assemblies of GaAs photoelectrodes with decoupled optical and reactive interfaces for unassisted solar water splitting. *Nat. Energy* **2**, 1-5 (2017).

- 117 Gai, B. *et al.* Printed assemblies of microscale triple-junction inverted metamorphic GaInP/GaAs/InGaAs solar cells. *Prog Photovolt Res Appl.* **27**, 520-527 (2019).
- 118 Chen, H. *et al.* A polymeric planarization strategy for versatile multiterminal electrical transport studies on small, bulk crystals. *ACS Appl. Electron. Mater.* **4**, 5550-5557 (2022).
- 119 Chen, H. & Ravichandran, J. A system built for both deterministic transfer processes and contact photolithography. *Adv. Eng. Mater.* **26**, 2401228 (2024).
- 120 Naito, M. & Tanaka, S. Electrical transport properties in  $2H$ -NbS<sub>2</sub>, -NbSe<sub>2</sub>, -TaS<sub>2</sub> and -TaSe<sub>2</sub>. *J. Phys. Soc. Jpn.* **51**, 219-227 (1982).
- 121 Zhu, X. *et al.* Classification of charge density waves based on their nature. *Proc. Natl. Acad. Sci.* **112**, 2367-2371 (2015).
- 122 Berglund, C. & Guggenheim, H. Electronic properties of VO<sub>2</sub> near the semiconductor-metal transition. *Phys. Rev.* **185**, 1022 (1969).
- 123 Rosevear, W. & Paul, W. Hall effect in VO<sub>2</sub> near the semiconductor-to-metal transition. *Phys. Rev. B* **7**, 2109 (1973).
- 124 Ko, C. & Ramanathan, S. Observation of electric field-assisted phase transition in thin film vanadium oxide in a metal-oxide-semiconductor device geometry. *Appl. Phys. Lett.* **93**, 252101 (2008).
- 125 Kucharczyk, D. & Niklewski, T. Accurate X-ray determination of the lattice parameters and the thermal expansion coefficients of VO<sub>2</sub> near the transition temperature. *J. Appl. Crystallogr.* **12**, 370-373 (1979).
- 126 Di Salvo, F. & Graebner, J. The low temperature electrical properties of  $1T$ -TaS<sub>2</sub>. *Solid State Commun.* **23**, 825-828 (1977).



- 127 Driscoll, T. *et al.* Phase-transition driven memristive system. *Appl. Phys. Lett.* **95**, 043503 (2009).
- 128 Jackson, J. & Shaw, M. The form and stability of current-voltage characteristics for ideal thermal switching. *Appl. Phys. Lett.* **25**, 666-668 (1974).
- 129 Taketa, Y. *et al.* New oscillation phenomena in VO<sub>2</sub> crystals. *Appl. Phys. Lett.* **27**, 212-214 (1975).
- 130 Kumar, S. *et al.* Local temperature redistribution and structural transition during joule-heating-driven conductance switching in VO<sub>2</sub>. *Adv. Mater.* **25**, 6128-6132 (2013).
- 131 Del Valle, J. *et al.* Subthreshold firing in Mott nanodevices. *Nature* **569**, 388-392 (2019).
- 132 Vaskivskiy, I. *et al.* Fast electronic resistance switching involving hidden charge density wave states. *Nat. Commun.* **7**, 1-6 (2016).
- 133 Mohammadzadeh, A. *et al.* Evidence for a thermally driven charge-density-wave transition in 1T-TaS<sub>2</sub> thin-film devices: Prospects for GHz switching speed. *Appl. Phys. Lett.* **118**, 093102 (2021).
- 134 Lee, Y. W. *et al.* Metal-insulator transition-induced electrical oscillation in vanadium dioxide thin film. *Appl. Phys. Lett.* **92**, 162903 (2008).
- 135 Seo, G. *et al.* Experimental investigation of dimension effect on electrical oscillation in planar device based on VO<sub>2</sub> thin film. *Thin Solid Films* **519**, 3383-3387 (2011).
- 136 Beaumont, A. *et al.* Current-induced electrical self-oscillations across out-of-plane threshold switches based on VO<sub>2</sub> layers integrated in crossbars geometry. *J. Appl. Phys.* **115**, 154502 (2014).
- 137 Kumar, S. *et al.* Dynamical memristors for higher-complexity neuromorphic computing. *Nat. Rev. Mater.* **7**, 575-591 (2022).

- 138 Kumar, S. *et al.* Chaotic dynamics in nanoscale NbO<sub>2</sub> Mott memristors for analogue computing. *Nature* **548**, 318-321 (2017).
- 139 Yi, W. *et al.* Biological plausibility and stochasticity in scalable VO<sub>2</sub> active memristor neurons. *Nat. Commun.* **9**, 4661 (2018).
- 140 Kang, J.-H. *et al.* Monolithic 3D integration of 2D materials-based electronics towards ultimate edge computing solutions. *Nat. Mater.* **22**, 1470-1477 (2023).
- 141 Pendurthi, R. *et al.* Monolithic three-dimensional integration of complementary two-dimensional field-effect transistors. *Nat. Nanotechnol.* **19**, 970-977 (2024).
- 142 Jia, L. *et al.* Fabrication technologies for the on-chip integration of 2D materials. *Small Methods* **6**, 2101435 (2022).

# TOC

